IEEE Open Journal of the Communications Society

Sparse Channel Estimation for Visible Light Optical OFDM Systems Relying on Bayesian Learning

SHUBHAM SAXENA[1] (Graduate Student Member, IEEE), SURAJ SRIVASTAVA[1] (Member, IEEE), SAURABH SHARMA[1], ADITYA K. JAGANNATHAM[1] (Senior Member, IEEE), AND LAJOS HANZO[2] (Life Fellow, IEEE)

[1]Department of Electrical Engineering, Indian Institute of Technology Kanpur, Kanpur 208016, India
[2]School of Electronics and Computer Science, University of Southampton, Southampton SO17 1BJ, U.K.

CORRESPONDING AUTHOR: L. HANZO (e-mail: lh@ecs.soton.ac.uk).

The work of Aditya K. Jagannatham was supported in part by the Qualcomm Innovation Fellowship, and in part by the Arun Kumar Chair Professorship. L. Hanzo would like to acknowledge the financial support of the Engineering and Physical Sciences Research Council projects EP/W016605/1, EP/X01228X/1, and EP/Y026721/1 as well as of the European Research Council's Advanced Fellow Grant QuantCom (Grant No. 789028).

ABSTRACT Sparse multipath channel impulse response (CIR) estimation schemes are conceived for optical orthogonal frequency division multiplexing (O-OFDM) visible light communication (VLC) systems. We commence by deriving the input-output models for both asymmetrically clipped optical OFDM (ACO-OFDM) and direct current-biased optical OFDM (DCO-OFDM) systems. A multipath CIR model is derived that captures both the diffusive as well as specular reflections of the VLC channel. Next, we introduce both the sparsity-agnostic conventional least square (LS) and the linear minimum mean square error (LMMSE) channel estimation (CE) techniques. This is followed by the orthogonal matching pursuit (OMP)-based sparse recovery technique, which exploits the delay-domain sparsity of the CIR. Furthermore, a novel sparse multipath CIR estimation scheme is proposed using the Bayesian learning (BL) framework, which requires only a limited number of pilot subcarriers, hence resulting in a reduced pilot overhead as compared to other state-of-the-art (SoA) CE techniques. The Bayesian Cramer Rao lower bound (BCRLB) as well as the Oracle-minimum mean squared error (O-MMSE) estimator are also derived for benchmarking the estimation performance of the proposed BL-based framework. Our simulation results demonstrate that the proposed BL method outperforms other existing sparse and conventional CE methods in terms of various metrics, such as the normalized mean-square-error (NMSE), the outage probability (OP), and the bit error-rate (BER) despite its reduced pilot overhead.

INDEX TERMS Bayesian learning (BL), BCRLB, channel estimation (CE), expectation maximization, visible light communication.

I. INTRODUCTION

THE current radio-frequency (RF) spectral bands have limited time-frequency resources to fulfil the ever-growing mobile data traffic demands, resulting in an impending spectral bottleneck in next-generation wireless communication systems. To overcome this barrier, visible light communication (VLC), which operates in the currently underutilized 400 THz to 800 THz frequency band, has evolved as a viable substitute to conventional RF-based wireless communication systems, particularly for indoor scenarios [1]–[3]. To achieve the dual objectives of communication and illumination, VLC employs light-emitting diodes (LEDs) wherein the intensity modulation occurs at a rate that is imperceivable by the human eyes. Compared to traditional RF systems, VLC offers various benefits, including improved security, reduced biological effects due to radiation, energy efficiency, and a superior signal-to-noise ratio (SNR) [1], [4]. Hence, the energy efficiency and low cost of LEDs render VLC a promising green technology for next generation communication systems [5].

The channel in VLC is comprised of line-of-sight (LoS) and non-line-of-sight (NLoS) paths. The LoS path is the direct path from the LED source to the photodetector (PD) receiver, whereas the NLoS paths are created when the

transmitted light from the LED source reaches the PD of the receiver after reflecting off the walls, objects, and other surfaces. This multipath propagation results in the time dispersion of the received signal. The power delay profile of this is analyzed in [6]. The resultant delay spread introduces inter-symbol interference (ISI) in indoor VLC systems [7], [8]. Hence optical orthogonal frequency division multiplexing (O-OFDM) has attracted the interest of several researchers as a viable technique for multicarrier modulation that can be implemented in LED-based VLC systems, as a benefit of its ability to reduce the ISI, while achieving excellent spectral efficiency [4], [9]. In contrast to typical RF OFDM systems, the modulation of O-OFDM VLC systems relies on the intensity modulation and direct detection (IM/DD) technology [10]. Since in IM/DD the modulated signal can only be non-negative and real-valued, an O-OFDM system typically employs either asymmetrically clipped optical OFDM (ACO-OFDM) modulation [11] or direct current-biased optical OFDM (DCO-OFDM) modulation [12]. The primary difference between the above two modulation schemes is that while in DCO-OFDM a DC bias is added to the transmitted signals to produce unipolar signals, in ACO-OFDM modulation the initial bipolar O-OFDM signals is clipped at zero and thus the resultant unipolar signal contains the positive components only. This property makes the ACO-OFDM technique more energy-efficient than the DCO-OFDM scheme [9], [10]. However, it must also be noted that a DCO-OFDM system uses half of the available subcarriers, whereas its ACO-OFDM counterpart can only use half the number of odd subcarriers to communicate the data symbols. This leads to improved spectral efficiency for the DCO-OFDM technology [9], [10]. Thus, these competing approaches for VLC systems strike a different compromise across the optical energy and spectral efficiency (ESE). It is important to note that the O-OFDM-VLC system's performance critically depends on the equalization at the receiver to overcome the impact of interference arising from natural light sources, background noise as well as the multipath propagation of the channel. Therefore, channel estimation (CE) is the key to achieve the best performance, thus reaping the potential benefits of O-OFDM-VLC communication, which forms the focus of this work. Furthermore, in light of the above discussion pertaining to the advantageous aspects of both the DCO-OFDM as well as ACO-OFDM approaches, our work considers both these modulation schemes. The existing contributions in this context are critically appraised in the subsequent section.

A. Literature review

The traditional CE techniques of VLC systems include pilot-assisted linear minimum mean square error (LMMSE) and least squares (LS) techniques. The authors of [13] employed the LS and LMMSE algorithms, respectively, for CE in O-OFDM-VLC for channels associated with $L_h = 6$ taps, where L_h denotes the length of the VLC CIR. The LS technique is perhaps the easiest to implement, although it is highly susceptible to noise [13]. On the other hand, the LMMSE offers a more precise estimate of the channel state information (CSI) than the LS, but has a slightly higher complexity [13]. In [14] the authors examined higher-order reflections in multipath VLC systems for high data rate systems. In fact, their findings suggest that conventional VLC channel models, which consider only the first few reflections, do not provide sufficient accuracy for high-rate VLC systems. Gong and Xu [15] perform CE using the LS technique and correlator banks followed by signal detection using the LMMSE receiver and maximum likelihood sequence detection (MLSD) schemes. Moreover, the system model therein considers only NLoS components. A modified zero-correlation-code pair based algorithm designed for the estimation of the channel parameters of a multipath VLC channel was analysed by the authors of [16]. Haigh *et al.* [17] conceived artificial neural networks (ANN) and adaptive decision feedback equalization for VLC systems. However, the ANN proposed in [17] is challenging to implement due to its hardware complexity and the technique advocated relies on simplistic on-off keying (OOK) modulation, that restricts its general applicability. A novel CE technique was developed in [18], where O-OFDM was employed to eliminate the multipath interference in a VLC system having a CIR of $L_h = 32$ taps. Lee *et al.* [19] employed a deep neural network (DNN)-based framework for dimmable VLC systems, where the encoder and decoder pair is replaced by a DNN-based VLC transceiver. However, their simulations were performed only for OOK modulated VLC systems. The authors of [20] designed transceivers for multi-coloured VLC systems using a deep learning (DL)-based scheme. Similarly, Wang *et al.* [21] designed a DL-based detector for generalized spatial modulation (GenSM) in VLC systems. However, the system model of [20] and [21] only considers a LoS VLC channel model. Yang *et al.* [22] extended the traditional RF-OFDM-based CE techniques to VLC systems by considering a multipath CIR model for DCO-OFDM systems. Zhang *et al.* [23] presented a novel adaptive CE scheme that employs the least squares discrete Fourier transform (LS-DFT) combined with the orthogonal matching pursuit (OMP) algorithm, wherein the authors initially estimate the VLC channel gains utilising the LS estimate, and subsequently employ the cubic B-spline interpolation technique for estimation of the subchannels across all subcarriers. Finally, the resultant data is subjected to the DFT to get the frequency-domain (FD) CSI. However, the BER performance of their suggested technique is not optimal across the entire SNR range. Explicitly, the LS-DFT performs better in the low SNR regime, while the OMP yields an improved performance in the high-SNR range. Notably, the practical VLC channel model, described in [8], [18], [24] is more sophisticated, because it comprises a LoS component as well as several NLoS components.

TABLE 1: Boldly contrasting our contributions to the current state-of-the-art

Features	[18]	[19]	[25]	[26]	[27]	[28]	[29]	[30]	[31]	[32]	[33]	**Proposed**
DCO-OFDM	✓				✓	✓		✓	✓		✓	✓
ACO-OFDM			✓				✓			✓		✓
LoS with NLoS channel model	✓	✓	✓	✓				✓		✓		✓
BL-based CE											✓	✓
BCRLB/CRLB	✓				✓							✓
FOCUSS												✓
Sparse CIR and OMP			✓		✓	✓	✓	✓				✓
Oracle MMSE												✓
Perfect CSI	✓				✓					✓	✓	✓

Interestingly, the small number of multipath components, in comparison to the large delay spread results in the VLC channel being sparse in the delay domain [23], [25], [27]–[30], [34]–[36]. Therefore, sparsity-based CE techniques can lead to a significant increase in estimation accuracy as compared to the conventional LMMSE and LS algorithms [29]. Several researchers have tried to enhance the accuracy of CE in VLC systems by leveraging this sparsity, which includes various cutting edge sparse signal recovery algorithms, namely the OMP and its variants. Zhao *et al.*, in their seminal paper [29] employed the OMP scheme relying on a partially superimposed training sequence for CE in an ACO-OFDM VLC system, with an L_h as high as 80, while setting the CIR coefficients having magnitudes lower than 10^{-4} to zero. The authors of [28] used the estimation of signal parameters via rotational invariance technique (ESPRIT) for determining the multipath parameters, which are then used to build the dictionary matrix. Following this, the basis pursuit denoising (BPDN) algorithm [28] was used in their work for the reconstruction of the VLC channel frequency response (CFR). However, only NLoS optical wireless communication was considered in their channel model, and the O-OFDM modulation schemes used were not specified. The authors of [33] consider sparse Bayesian relevance vector machine (RVM) regression-based CE for OFDM-VLC systems using complex training symbols, while considering only the optical LoS channel gain. However, their results are only validated for DCO-OFDM systems, with the constraint that the real and imaginary parts of the transmitted training symbols are identical, which limits the applicability of their work. Moreover, closed-form expressions for performance benchmarks such as the Bayesian Cramer-Rao lower bound (BCRLB) and Oracle-MMSE (O-MMSE) estimator are not derived in [33]. Niaz *et al.* [25] reported a self-aware step size sparsity adaptive matching pursuit (SS-SAMP) technique for CE in an ACO-OFDM system, that offers superior performance in terms of BER and minimum mean square error (MMSE) compared to the conventional CE approaches of VLC systems. In [37], Manur and Ali extended the concept of [25] to MIMO-ACO-OFDM systems using the dynamic step-size sparsity adaptive matching pursuit (DSS-SAMP) technique for both spatially multiplexed (SM) and for space-time block coded (STBC) VLC systems. A key drawback of the proposed techniques of [25] and [37] is that their performance depends on the choice of thresholds utilized, which must be empirically adjusted for best results. Furthermore, the performance of their proposed algorithms is dependent on the choice of the measurement matrix. Thus, the performance of a majority of the sparse estimation techniques proposed in the existing VLC literature, is dependent on the specific choice of the dictionary/measurement matrix and the particular stopping criterion employed. However, they tend to lead to convergence errors and significant performance degradation [25], [38]. To overcome these shortcomings of the state-of-the-art (SoA) sparse CE algorithms, we propose a novel BL-based sparse multipath CIR estimation technique for O-OFDM-VLC systems, considering both the popular ACO/ DCO-OFDM modulation formats. Compared to existing sparse recovery techniques, such as OMP and FOCal Underdetermined System Solver (FOCUSS) [38], [39], the proposed BL-based approach is shown to yield significantly improved estimates. The main contributions of this treatise are summarized below.

B. Contributions of the work

1) A sparse multipath CIR model is developed for wideband VLC channels by incorporating both the diffusive as well as specular reflections along with the attributes of the optical reflectors, source, and receiver.
2) Commencing from the popular LS and LMMSE based CE, we develop a CE model, which justifies the delay domain sparsity of the CIR in VLC systems. This is followed by the OMP based sparse recovery technique, which exploits the resultant CIR sparsity, albeit facing several drawbacks.
3) Subsequently, a novel sparse multipath CIR CE is conceived using the novel BL framework for O-OFDM-VLC systems. The proposed BL-based CE technique requires only a limited number of pilot subcarriers, hence resulting in an enhanced spectral efficiency and

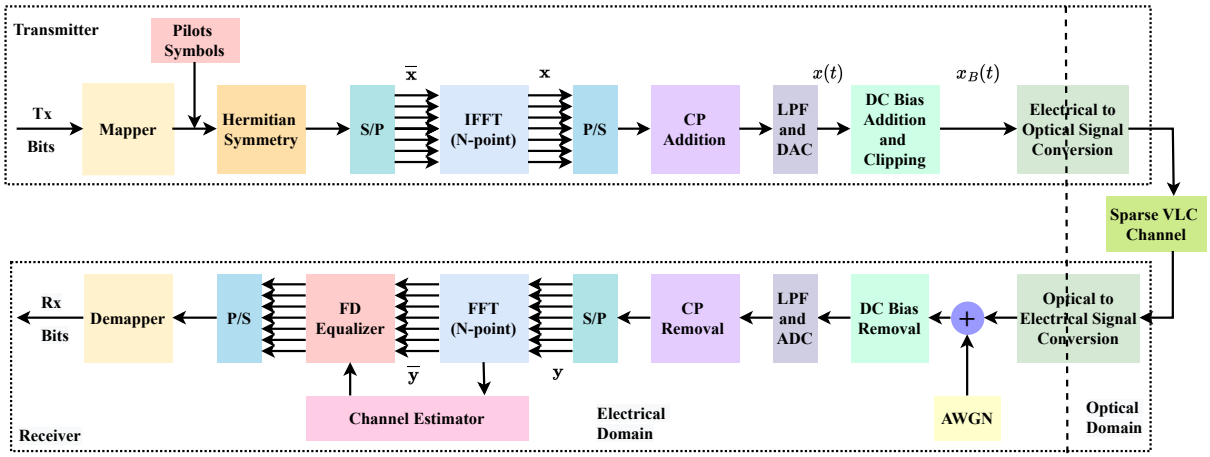

FIGURE 1: Schematic diagram of a DCO-OFDM transmitter and receiver.

reduced pilot overhead (ρ) in contrast to the current CE approaches. Furthermore, the proposed technique is free of tuning/regularization parameters and has a robust convergence.

4) Closed-form expressions are derived for the BCRLB and O-MMSE estimator to benchmark the performance of the BL-based technique conceived for sparse VLC CE.
5) The efficacy of the proposed BL-based CE approach is exhaustively evaluated for both DCO-OFDM and ACO-OFDM for different simulation environments, in terms of several metrics, which include the bit-error-rate (BER), outage probability (OP), normalized mean squared error (NMSE), and the pilot overhead along with the complexity analysis and speed of convergence of the proposed BL-based CE technique.

C. Organization of the paper

The rest of this paper is arranged as follows. Section-II examines the DCO-OFDM and ACO-OFDM system models. Section-III investigates the multipath channel model, which includes both diffusive as well as specular reflections of the VLC channel, followed by Section-IV that presents our OMP-based greedy technique developed for sparse VLC CE. Section-V develops the proposed novel BL-based CE technique along with the relevant performance benchmarks such as the O-MMSE estimator and a lower bound on the MMSE given by the BCRLB. Section-VI includes the simulation results characterizing the performance of the proposed sparse CE techniques in comparison to the existing benchmarks. Section-VII offers our conclusions.

Notations: The following notations are used throughout this paper: Uppercase boldface letters such as $\mathbf{A}$ denote matrices, while lowercase boldface letters such as $\mathbf{a}$ denote vectors. The operators $(\cdot)^*, (\cdot)^T, (\cdot)^{-1}, (\cdot)^H$, and $(\cdot)^\dagger$ represent the conjugate, transpose, inverse, Hermitian, and pseudoinverse of a matrix, respectively. $\mathbb{C}^{M\times N}, \mathbb{R}^{M\times N}$, and $\mathbb{R}_+^{M\times N}$ are the sets of $M \times N$ matrices, whose elements are complex-valued, real-valued, and non-negative real-valued, respectively. The operator $\mathbb{E}\{\cdot\}$ represents the statistical expectation, $\text{diag}\{\mathbf{a}\}$ represents a diagonal matrix with $\mathbf{a}$ on its principal diagonal, and $\arg f(\cdot)$ denotes the argument of the function $f(\cdot)$. $\mathbf{I}_N$ is the $N \times N$ identity matrix while $|\cdot|, ||\cdot||$, and $||\cdot||_p$ represent the scalar magnitude, vector norm, and l_p norm, respectively. Furthermore, $\mathbf{M}(i,:)$ and $\mathbf{M}(:,j)$ represent the i^{th} row and j^{th} column of the matrix $\mathbf{M}$. The function $\det(\cdot)$ represents the determinant of the corresponding matrix and $\text{Re}(\cdot)$ denotes the real part of a complex number. The quantity $\tilde{(\cdot)}$ denotes a variable in FD, $\overline{(\cdot)}$ denotes a vector in FD, and $\widehat{(\cdot)}$ denotes an estimate of the variable. The signal $\text{rect}(x)$ is defined as,

$$\text{rect}(x) = \begin{cases} 1, & \text{if } |x| \leq 1, \\ 0, & \text{if } |x| > 1. \end{cases}$$

II. Optical OFDM System Models

Optical OFDM systems are significantly different from conventional RF-based OFDM systems, since the former modulates the intensity of LEDs, which constrains the waveform to be non-negative as well as real-valued. Again, the two most popular schemes for optical modulation are ACO-OFDM and DCO-OFDM, which are briefly touched upon next.

A. DCO-OFDM system model

A serial bit sequence is mapped to N complex-valued symbols that belong to a digital constellation such as quadrature amplitude modulation (QAM), where N denotes the number of subcarriers. Figure 1 depicts the DCO-OFDM transceiver. The complex-valued data vector can be represented as follows: $\overline{\mathbf{x}} = [\tilde{x}_0, \tilde{x}_1, \tilde{x}_2, \ldots, \tilde{x}_{N-1}]^T \in \mathbb{C}^{N\times 1}$, where $\tilde{x}_0 = \tilde{x}_{N/2} = 0$ to avoid the DC component, and the symbols $\tilde{x}_1$ to $\tilde{x}_{N/2-1}$ satisfy the symmetry property $\tilde{x}_j = \tilde{x}^*_{N-j}$, for $N/2+1 \leq j \leq N-1$ [40], [41]. The N-point inverse fast Fourier transform (IFFT) is subjected to the vector $\overline{\mathbf{x}}$ to produce the real-valued time-domain (TD) signal,

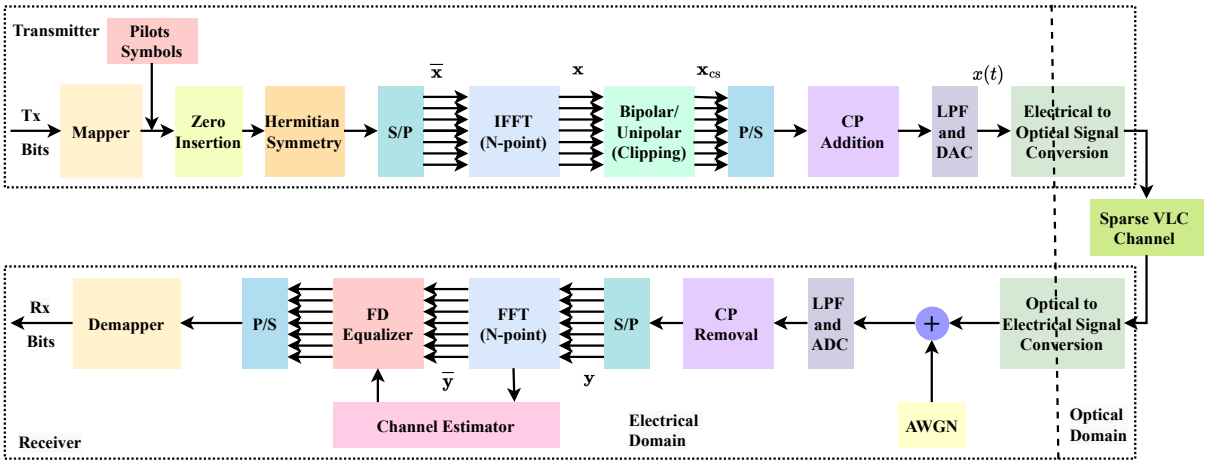

FIGURE 2: Schematic diagram of an ACO-OFDM transmitter and receiver.

which can be modeled as $\mathbf{x} = \mathbf{W}\bar{\mathbf{x}}$, where $\mathbf{W}$ denotes the $N \times N$ IDFT matrix defined as $\mathbf{W} = \{w_{n,k}\}_{n,k=0}^{N-1} \in \mathbb{C}^{N\times N}$ and $w_{n,k} = \frac{1}{N} e^{j\left(\frac{2\pi nk}{N}\right)}$. Thus, the n^{th} component x_n of the TD signal $\mathbf{x}$ is obtained as

$$\begin{aligned} x_n &= \frac{1}{N}\sum_{k=0}^{N-1} \tilde{x}_k e^{\left(j\frac{2\pi kn}{N}\right)} \\ &= \frac{1}{N}\sum_{k=1}^{N/2-1} \left(\tilde{x}_k e^{\left(j\frac{2\pi kn}{N}\right)} + \tilde{x}_{N-k} e^{\left(j\frac{2\pi (N-k)n}{N}\right)}\right) \\ &= \frac{1}{N}\sum_{k=1}^{N/2-1} \left(\tilde{x}_k e^{\left(j\frac{2\pi kn}{N}\right)} + \tilde{x}_k^* e^{\left(-j\frac{2\pi kn}{N}\right)}\right) \\ &= \frac{2}{N}\sum_{k=1}^{N/2-1} \text{Re}\left(\tilde{x}_k e^{\left(j\frac{2\pi kn}{N}\right)}\right). \end{aligned} \tag{1}$$

The TD signal ($\mathbf{x}$) is converted with the aid of a parallel-to-serial (P/S) converter to a serial stream, followed by the addition of a cyclic prefix (CP) of length L_{CP}. Note that in order to remove the ISI, L_{CP} must be longer than the delay spread of the multipath VLC channel. The signal is then passed through both a digital to analog converter (DAC) and a low pass filter (LPF) that produces the waveform $x(t)$. Since $x(t)$ is bipolar in nature, to render it compatible with intensity modulation, a DC bias (B_{DC}) is introduced in $x(t)$, where $\text{B}_{\text{DC}} = \upsilon\sqrt{\mathbb{E}\{x^2(t)\}}$, and υ is a constant [40], [41]. In the literature, B_{DC} is typically set as $10\log(\upsilon^2+1)$ [12]. Thus, the unipolar signal $x_B(t)$ is obtained as follows [2]:

$$x_B(t) = x(t) + \text{B}_{\text{DC}}. \tag{2}$$

Furthermore, any negative clip after the addition of B_{DC} is forced to zero. The resultant DCO-OFDM signal is then transformed to an optical signal and transmitted over the multipath VLC channel, which can be represented by the CIR vector $\mathbf{h} = [h(0), h(1), \ldots, h(L_h-1)]^T \in \mathbb{R}_+^{L_h\times 1}$, where L_h is the order of the VLC CIR [4]. After CP removal, serial to parallel (S/P) combiner and the fast Fourier transform (FFT) based demodulation at the receiver, the input/output (i/o) model of the signal received at the k^{th} subcarrier becomes [4]:

$$\tilde{y}_k = \tilde{h}_k \tilde{x}_k + \tilde{w}_k, \quad k = 1, \ldots, N-1, \tag{3}$$

where $\tilde{w}_k$ is the zero-mean complex additive white Gaussian noise (AWGN) that has a variance of σ^2_{AWGN} [42], and the VLC channel transfer function is given by, $\tilde{h}_k = \sum_{n=0}^{L_h-1} h(n) e^{\frac{-j2\pi nk}{N}}$. The vector representation $\overline{\mathbf{y}} = [\tilde{y}_0, \tilde{y}_1, \ldots, \tilde{y}_{N-1}]^T$ of the FFT output can be described as

$$\overline{\mathbf{y}} = \text{diag}\{\overline{\mathbf{h}}\}\overline{\mathbf{x}} + \overline{\mathbf{w}}, \tag{4}$$

where $\overline{\mathbf{w}} = [\tilde{w}_0, \tilde{w}_1, \ldots, \tilde{w}_{N-1}]^T$ and $\overline{\mathbf{h}} = [\tilde{h}_0, \tilde{h}_1, \ldots, \tilde{h}_{N-1}]^T$ [4]. In the TD, VLC systems are affected by both thermal and shot noise. Their cumulative effect can be modeled by AWGN of variance $\sigma^2_{\text{VLC}} = \sigma^2_{\text{Shot}} + \sigma^2_{\text{Thermal}}$, where $\sigma^2_{\text{Shot}} = 2qR[P_S(t) + P_D]$ and $\sigma^2_{\text{Thermal}} = \frac{4k_bBT}{r}$ [18], [43], [44]. The quantity q represents electron charge, r is the input resistance, $P_S(t)$ is the instantaneous received power, R denotes the PD responsivity, B is the bandwidth, T represents the temperature, k_b denotes Boltzmann's constant, and P_D is the mean power received in an indoor environment from diffuse sunlight. The FD equivalent of the above VLC noise can be approximated by AWGN, whose variance is given by $\sigma^2_{\text{AWGN}} = 2qRN(P_R + P_D) + N\sigma^2_{\text{Thermal}}$, where P_R is the mean optical power within the room [18]. Similar to conventional OFDM, in a DCO-OFDM VLC system, single tap FD equalization may be used for recovering the FD symbols $\widehat{x}_k$. Each subcarrier is subsequently input to a demodulator that maps the complex symbol estimates $\widehat{x}_k$ to a set of information bits to retrieve the transmitted data.

B. ACO-OFDM system model

Figure 2 shows a schematic representation of an ACO-OFDM transceiver. The primary difference between the DCO-OFDM and ACO-OFDM systems lies in the assignment of the data symbols to the subcarriers. In ACO-

OFDM, the data symbols are assigned to the odd subcarriers of the first $N/2$ subcarriers in a Hermitian symmetric fashion, similar to a DCO-OFDM system. Thus, the ACO-OFDM system carries only $N/4$ information symbols. Therefore, the IFFT based modulator's input has the form, $\overline{\mathbf{x}} = [0, \tilde{x}_1, 0, \tilde{x}_3, \ldots, \tilde{x}_{N-1}]^T \in \mathbb{C}^{N\times 1}$, where $\tilde{x}_j = \tilde{x}^*_{N-j}$ for $N/2+1 \leq j \leq N-1$ [41], [45]. Note that the TD signal generated by the IFFT based modulator is real and anti-symmetric, i.e.,

$$x_n = \frac{1}{N}\sum_{k=0}^{N-1} \tilde{x}_k e^{\left(j\frac{2\pi kn}{N}\right)} = \frac{1}{N}\sum_{m=0}^{N/2-1} \tilde{x}_{2m+1} e^{\left(j\frac{2\pi(2m+1)n}{N}\right)}$$

$$= -\frac{1}{N}\sum_{m=0}^{N/2-1} \tilde{x}_{2m+1} e^{\left(j\frac{2\pi(2m+1)(n+N/2)}{N}\right)} = -x_{n+N/2}, \tag{5}$$

where $n = 0, 1, \ldots, N/2-1$. We observe from (5) that the first and second halves of the samples have identical amplitudes and opposite signs. Consequently, the negative valued samples, i.e., $x_n < 0$, are clipped to zero. Thus, there is no need for a DC bias to render it unipolar. The resultant clipped signal ($x_{n,\text{cs}}$) is as follows:

$$x_{n,\text{cs}} = \begin{cases} x_n, & \text{if } x_n > 0, \\ 0, & \text{if } x_n \leq 0. \end{cases} \tag{6}$$

The clipped TD signal is then passed to a P/S converter, which is followed by the CP addition, DAC conversion and LPF, ultimately resulting in $x(t)$. This is then optically modulated and transmitted through a multipath VLC channel [10]. The relationship between the FD clipped data symbols $\tilde{x}_{2m+1,\text{cs}}$ and the original data symbols $\tilde{x}_{2m+1}$ can be formulated as:

$$\begin{aligned} \tilde{x}_{2m+1,\text{cs}} &= \frac{1}{N}\sum_{n=0}^{N-1} x_{n,\text{cs}}\, e^{\left(-j\frac{2\pi(2m+1)n}{N}\right)} \\ &= \frac{1}{N}\sum_{n=0}^{N/2-1} (x_{n,\text{cs}} - x_{n+N/2,\text{cs}})\, e^{\left(-j\frac{2\pi(2m+1)n}{N}\right)} \\ &= \frac{1}{2N}\sum_{n=0}^{N/2-1} (x_n - x_{n+N/2})\, e^{\left(-j\frac{2\pi(2m+1)n}{N}\right)} \\ &= \frac{1}{2}\tilde{x}_{2m+1} \quad \text{,where} \quad m = 0, 1, \ldots, N/2-1. \end{aligned} \tag{7}$$

Thus, due to clipping, at the odd subcarriers the magnitudes of the FD clipped data symbols after FFT are reduced to half the magnitudes of the corresponding original data symbols [4], [10]. Therefore, the receiver side processing of an ACO-OFDM system is identical to that of its DCO-OFDM counterpart, with the exception that in the former, only the odd subcarriers are retrieved after the FFT based demodulation. The outputs are subsequently passed through the equalizer and demapper blocks. The next section outlines the model of a multipath VLC channel.

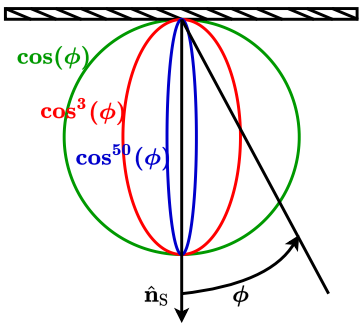

FIGURE 3: The generalized Lambertian radiation lobes for mode numbers $l = 1, 3,$ and 50.

III. Multipath VLC Channel Model

This section defines the properties of the optical source, multipath VLC channel, reflector, and receiver. Typically, the LEDs serve as the optical sources that emit radiation according to the generalized Lambertian pattern $R_L(\phi)$ with uniaxial symmetry formulated as [12]

$$R_L(\phi) = \frac{l+1}{2\pi} P_S \cos^l(\phi) \quad \text{for} \quad \phi \in [\, -\pi/2, \pi/2\,], \tag{8}$$

where l represents the mode number corresponding to the particular radiating lobe, P_S represents the optical sources radiated power, and ϕ is the source irradiance angle with regard to the unit-length vector $\hat{\mathbf{n}}_\text{S}$, which is normal to the radiation surface. As illustrated in Figure 3, the mode number l defines the form of the radiation lobe and the directionality of the radiation source. Thus, a large mode number signifies a higher directionality, while the mode number $l = 1$ pertains to a generalized Lambertian source. The maximum radiation intensity is obtained at $\phi = 0°$, and thus, $R_{L,\text{max}}(\phi) = \frac{l+1}{2\pi}P_S$. The semi-angle at half of the maximum radiation intensity is given by $\phi_{1/2} = \arg(R_L(\phi) = R_{L,\text{max}}/2) = \cos^{-1}(2^{-1/l})$. In general, we characterize any optical point source by the ordered three-tuple $\text{S} = \{\mathbf{r}_\text{S}, \hat{\mathbf{n}}_\text{S}, l\}$, where $\mathbf{r}_\text{S}$ represents the optical source position vector. Similarly, the optical receiver is characterized by the ordered four-tuple $\text{R} = \{\mathbf{r}_\text{R}, \hat{\mathbf{n}}_\text{R}, A_\text{R}, \Psi_\text{FoV}\}$, where $\mathbf{r}_\text{R}$ is the receiver's position vector, $\hat{\mathbf{n}}_\text{R}$ is a unit-length vector normal to the radiating surface, A_R is the area of the receiver, and the field-of-view (FoV) angle is given by Ψ_FoV. The light signal is detected by the receiver if the angle of incidence (Ψ) (with regard to $\hat{\mathbf{n}}_\text{R}$) is lower than Ψ_FoV. Let the refractive index of the optical concentrator be given by μ. Generally, a non-imaging concentrator is utilized to boost the received signal intensity, whose gain is given by [12] [46]

$$\text{g}(\Psi) = \begin{cases} \frac{\mu^2}{\sin^2\Psi_\text{FoV}}, & \text{if } 0 \leq \Psi \leq \Psi_\text{FoV}, \\ 0, & \text{if } \Psi > \Psi_\text{FoV}, \end{cases} \tag{9}$$

where $\Psi_\text{FoV} \leq \pi/2$. The reflector model can be described with the aid of the source and receiver models. In the literature [12], reflecting materials such as walls, tiles, wood, and carpets are typically approximated as Lambertian. Thus, the

differential reflecting element (ε) first behaves as a receiver associated with the ordered four-tuple $\{\mathbf{r}_\varepsilon, \hat{\mathbf{n}}_\varepsilon, A_\varepsilon, \pi/2\}$. Subsequently, it behaves as a source with the ordered three-tuple $\{\mathbf{r}_\varepsilon, \hat{\mathbf{n}}_\varepsilon, 1\}$. The incident power is P_ε and the radiated power is ρP_ε, where the reflecting element's reflection coefficient is ρ. Thus, the reflector typically attenuates the power by a factor of ρ, where $0 < \rho < 1$ [12].

The multipath VLC channel is characterized by both a LoS as well as NLoS paths. Figure 4 shows the geometry of a single optical source (S_a), the receiver (R_b), and a pair of reflective elements ($\varepsilon_1, \varepsilon_2$) with a multipath VLC system for an indoor environment. The LoS path for any general source $S_a = \{\mathbf{r}_a, \hat{\mathbf{n}}_a, l\}$ and any general receiver $R_b = \{\mathbf{r}_b, \hat{\mathbf{n}}_b, A_{R_b}, \Psi_{FoV}\}$ has an impulse response, which is approximated as a delayed and scaled Dirac delta function, given as [12], [46], [47]

$$h^{(0)}(t; S_a, R_b) = \frac{l_a + 1}{2\pi d_{a,b}^2} A_{R_b} \cos^{l_a}(\phi_{a,b}) \cos(\Psi_{a,b}) g(\Psi_{a,b}) \times \text{rect}\left(\frac{\Psi_{a,b}}{\Psi_{FoV,b}}\right) \delta\left(t - \frac{d_{a,b}}{c}\right), \tag{10}$$

where c denotes the speed of light, the FoV of R_b is $\Psi_{FoV,b}$, A_{R_b} represents the PD area, $d_{a,b}$ denotes the distance across S_a and R_b, $\delta(.)$ is the Dirac delta function. Furthermore, $\Psi_{a,b}$ is the angle of incidence at R_b, l_a represents the mode number of the radiation lobe of S_a, and $\phi_{a,b}$ is the irradiance from S_a, so that, $d_{a,b} = ||\mathbf{r}_a - \mathbf{r}_b||$, $\cos(\phi_{a,b}) = \hat{\mathbf{n}}_a.(\mathbf{r}_a - \mathbf{r}_b)/d_{a,b}$, $\cos(\Psi_{a,b}) = \hat{\mathbf{n}}_b.(\mathbf{r}_a - \mathbf{r}_b)/d_{a,b}$.

In the NLoS path, light travels from the optical source to the receiver's photodetector (PD) through multiple reflections. The impulse response of the NLoS rays spanning from S_a to R_b is composed of $k+1$ paths, where the number of reflections is k. The impulse response of the link spanning from S_a to the first reflection ($\varepsilon_1 = \{\mathbf{r}_1, \hat{\mathbf{n}}_1, A_{\varepsilon_1}, \pi/2\}$) as shown in Figure 4 is given by [46]

$$h^{(0)}(t; S_a, \varepsilon_1) = \frac{l_a + 1}{2\pi d_{a,1}^2} A_{\varepsilon_1} \cos^{l_a}(\phi_{a,1}) \cos(\Psi_{a,1}) \times \text{rect}\left(\frac{\Psi_{a,1}}{\pi/2}\right) \delta\left(t - \frac{d_{a,1}}{c}\right). \tag{11}$$

The successive LoS reflections from the reflective element ($\varepsilon_j = \{\mathbf{r}_j, \hat{\mathbf{n}}_j, 1\}$) to the reflective element ($\varepsilon_k = \{\mathbf{r}_k, \hat{\mathbf{n}}_k, A_{\varepsilon_k}, \pi/2\}$) yields the corresponding impulse response formulated as

$$h^{(0)}(t; \varepsilon_j, \varepsilon_k) = \frac{1}{\pi d_{j,k}^2} A_{\varepsilon_k} \cos(\phi_{j,k}) \cos(\Psi_{j,k}) \times \text{rect}\left(\frac{\Psi_{j,k}}{\pi/2}\right) \delta\left(t - \frac{d_{j,k}}{c}\right). \tag{12}$$

Finally, the last reflection from ($\varepsilon_q = \{\mathbf{r}_q, \hat{\mathbf{n}}_q, 1\}$) to R_b yields the impulse response

$$h^{(0)}(t; \varepsilon_q, R_b) = \frac{1}{\pi d_{q,b}^2} A_{R_b} \cos(\phi_{q,b}) \cos(\Psi_{q,b}) g(\Psi_{q,b}) \times \text{rect}\left(\frac{\Psi_{q,b}}{\Psi_{FoV,b}}\right) \delta\left(t - \frac{d_{q,b}}{c}\right). \tag{13}$$

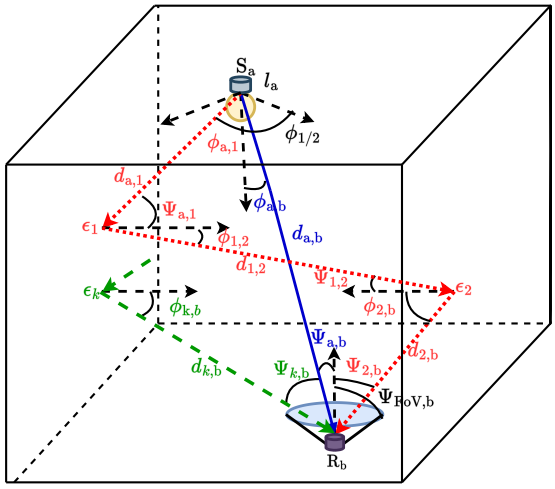

FIGURE 4: Geometry of the transmitter (LED), receiver (PD), and reflectors in a multipath VLC channel. The blue ("—") component represents the LoS path, red ("· · ·") ray represents the NLoS path considering a second-order reflection, and the k[th] order multipath is in green ("– –").

As illustrated in Figure 4, the NLoS path spanning from S_a to R_b after two reflections at ε_1 and ε_2 has the impulse response given by

$$h^{(2)}(t; S_a, \varepsilon_1, \varepsilon_2, R_b) = h^{(0)}(t; S_a, \varepsilon_1) \otimes \rho_1 h^{(0)}(t; \varepsilon_1, \varepsilon_2) \otimes \rho_2 h^{(0)}(t; \varepsilon_2, R_b), \tag{14}$$

where ρ_1 and ρ_2 are the reflectivities of the elements ε_1 and ε_2, respectively. Therefore, when there are M_r reflective elements and k reflections between S_a to R_b, the impulse response can be modeled as

$$h_{a\to b}^{(k)}(t; S_a, R_b) = \frac{l_a + 1}{2\pi} \sum_{i=1}^{M_r} \frac{A_i \rho_i}{d_{a,i}^2} \cos^{l_a}(\phi_{a,i}) \cos(\psi_{a,i}) \times \text{rect}\left(\frac{\psi_{a,i}}{\pi/2}\right) h^{(k-1)}\left(t - \frac{d_{a,i}}{c}; \varepsilon_i, R_b\right). \tag{15}$$

Finally, the impulse response representing K reflections between the a[th] source S_a and b[th] receiver R_b for the multipath VLC channel is the summation of the LoS impulse response (10) and NLoS (15) impulse responses, which is given by

$$h_{a\to b}(t; S_a, R_b) = h_{a\to b}^{(0)}(t; S_a, R_b) + \sum_{k=1}^{K} h_{a\to b}^{(k)}(t; S_a, R_b). \tag{16}$$

In the above expressions, $K = 0$ represents the LoS component of the channel, whereas $K \geq 1$ represents the NLoS components. Let the number of LED sources be denoted by N_{LED}. The multipath VLC channel spanning from all the

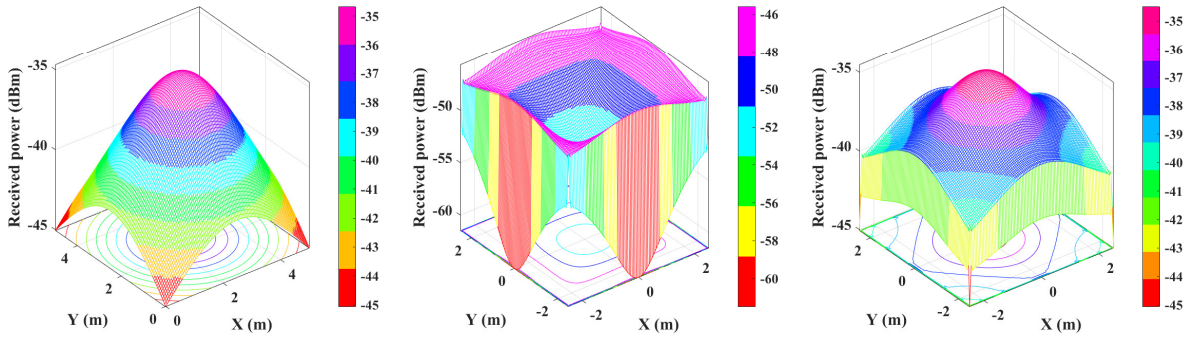

FIGURE 5: Received optical power distribution in a VLC system for a single illuminating source with $\mathfrak{g}(\Psi_{\mathrm{a,b}}) = 1$, $l_{\mathrm{a}} = 1$, and $\Psi_{\mathrm{FoV,b}} = 60^{\circ}$ for (a) an LoS path; (b) an NLoS path considering a first-order reflection and $\varrho = 0.8$; (c) LoS and NLoS paths considering first-order reflections and $\varrho = 0.8$.

LEDs to the receiver $\mathrm{R_b}$ can be represented as

$$h_b(t) = \sum_{i=1}^{N_{\mathrm{LED}}} \left[h^{(0)}_{i\to b}\left(t; \mathrm{S}_i, \mathrm{R_b}\right) + \sum_{k=1}^{K} h^{(k)}_{i\to \mathrm{b}}\left(t; \mathrm{S}_i, \mathrm{R_b}\right) \right]. \tag{17}$$

Furthermore, the average received optical power is P_R which is as follows $P_R = \tilde{h}_0 \times P_S$. Here, P_S denotes the average transmitted optical power and $\tilde{h}_0$ is the DC channel gain where, $\tilde{h}_0 = \int_{-\infty}^{\infty} h_b(t)\, dt$.

Figure 5 depicts the distribution of the optical power received from a single source of illumination. The optical power distribution for the LoS path is depicted in Figure 5a. The optical power distribution for the NLoS path considering first order multipath reflections from four of the walls is depicted in Figure 5b. Here each wall consist of M_r reflection grids with each grid having an area of A_{ε}, where $M_r = 4300$ and $A_{\varepsilon} = 0.0025$ m^2. Figure 5c shows the distribution of the optical power for the NLoS and LoS paths at the receiver, using the simulation parameters of Table 2.

IV. Sparse CE Model for VLC systems

This section describes the sparse multipath VLC channel model and CE techniques proposed in this work. In general, in an indoor environment, the light wave is diffusive in nature, which implies that it undergoes multiple internal reflections prior to reaching the receiver. Multipath reflections result in diffused rays that arrive at the receiver, in addition to the specular component of the signal. The multipath VLC channel can generally be described as [16], [48]

$$h(n) = \sum_{l=0}^{L_h-1} h(l)\delta\left(n - \nu_l\right), \tag{18}$$

where $h(l)$ is the VLC CIR coefficient and ν_l represents the propagation delay of the l^{th} transmission path. Typically, a significant fraction of the transmitted optical power is concentrated in the specular reflection, whereas the diffused reflection paths have lower optical power [23], [29]. As a result, the multipath VLC channel has a few paths having significant power, with little or no power in the rest [49]. Therefore, ignoring the insignificant channel paths can potentially enhance the CE performance. A thresholding technique can be employed to choose the most significant paths, with the gains of the other paths of negligible optical power set to zero [23]. Therefore, the multipath VLC channel can be regarded as a sparse channel [23], [25], [27]–[30], [35], [36]. Due to the increased attenuation of the longer paths, the amplitudes in a diffuse optical wireless channel tend to decay as the delay increases [48]. Hence, the TD CIR coefficient $h(l)$ of the l^{th} path can be modeled as an exponentially decaying function [13], [29], [50], [51]

$$h(l) = \frac{e^{-lt_s/\tau}}{\sum_{l=0}^{L_h-1} e^{-lt_s/\tau}}, \tag{19}$$

where τ represents the delay spread of the channel, which eventually relies on the average reflectivity of the surfaces and the size of the room, t_s represents the sampling period of the OFDM TD samples, and usually $\tau \in [0.5t_s, 1.5t_s]$ [48], [50], [52]. The values of $h(l)$ below 10^{-8} are assumed to be zeros [29]. The resultant s-sparse VLC CIR has a maximum of s non-zero coefficients, where $s << L_h$. Note that (17) describes the continuous TD channel response of the VLC system which comprises the LoS path and NLoS paths, whereas (18) describes the discrete-time domain model of the multipath VLC channel. Furthermore, (19) gives the model of the normalized samples of the TD CIR coefficients of the VLC system. Thus, (18) and (19) collectively define the sparse multipath CIR model of the VLC system. As emphasised at the beginning of this paper, CE and equalisation at the receiver side play a critical role in increasing the performance of O-OFDM-VLC systems. This motivates us to present novel CE models and schemes, which leverage the inherent sparsity of the multipath VLC channel.

Toward this, let the set of indices of the pilot subcarriers be defined as

$$P_I = \{I_0 + k \times I_P,\ k = 0, 1, \ldots, M_P/2 - 1\}, \quad (20)$$

where I_P is the interval between the pilot subcarriers, M_P denotes the number of pilots in an OFDM block satisfying the condition $(M_P/2-1)I_P < N/2$, and I_0 is the starting index of the pilot subcarriers. Hence, the pilot subcarrier indices can be described as $I_{\text{pilot}} = \{p|p \in P_I\} \cup \{p|N-p \in P_I\}$ and those of the data subcarriers belong to the set $I_{\text{data}} = \{0, 1, \ldots, N-1\} - I_{\text{pilot}}$. The FD channel transfer function is given by $\overline{\mathbf{h}} = \mathbf{Q}\mathbf{h}$, where $\mathbf{Q} \in \mathbb{C}^{N \times L_h}$ denotes the truncated DFT matrix associated with $Q_{k,l} = e^{-j\left(\frac{2\pi kl}{N}\right)}$, for $0 \leq k \leq N-1, 0 \leq l \leq L_h-1$. Let $\overline{\mathbf{x}} = [\tilde{x}_0, \tilde{x}_1, \ldots, \tilde{x}_{N-1}]^T \in \mathbb{C}^{N \times 1}$ represent the FD data vector having embedded pilots. The output after FFT at the receiver yields

$$\overline{\mathbf{y}} = \text{diag}\{\overline{\mathbf{h}}\}\overline{\mathbf{x}} + \overline{\mathbf{w}} = \text{diag}\{\overline{\mathbf{x}}\}\overline{\mathbf{h}} + \overline{\mathbf{w}} = \text{diag}\{\overline{\mathbf{x}}\}\mathbf{Q}\mathbf{h} + \overline{\mathbf{w}}. \quad (21)$$

The outputs corresponding to the pilot indices are obtained using the extraction matrix $\mathbf{E} \in \mathbb{R}_+^{M_P \times N}$, where $[\mathbf{E}]_{i,[I_{\text{pilot}}]_i} = 1$, with the rest of the elements being zero. This obeys $\mathbf{E}\mathbf{E}^H = \mathbf{I}_{M_P}$. The extraction matrix $\mathbf{E}$ is employed to select the M_P pilot outputs corresponding to the subcarrier indices I_{pilot}. The extracted pilot output vector $\overline{\mathbf{y}}_P = [\overline{\mathbf{y}}]_{I_{\text{pilot}}} \in \mathbb{C}^{M_P \times 1}$ can be modeled as

$$\overline{\mathbf{y}}_P = \text{diag}\{\overline{\mathbf{x}}_P\}\mathbf{E}\mathbf{Q}\mathbf{h} + \overline{\mathbf{w}}_P = \mathbf{B}\mathbf{h} + \overline{\mathbf{w}}_P, \quad (22)$$

where $\overline{\mathbf{x}}_P = [\overline{\mathbf{x}}]_{I_{\text{pilot}}} \in \mathbb{C}^{M_P \times 1}$ denotes the FD data vector having embedded pilots with the average pilot power set to $P_{\overline{x}}$, i.e., $\mathbb{E}[|\overline{\mathbf{x}}_P|^2] = P_{\overline{x}}$. Furthermore, $\mathbf{B} = \text{diag}\{\overline{\mathbf{x}}_P\}\mathbf{E}\mathbf{Q} \in \mathbb{C}^{M_P \times L_h}$ is the measurement matrix. The next section briefly highlights the conventional LS and LMMSE-based CE techniques used for estimating the multipath VLC CIR $\mathbf{h}$ from the pilot output $\overline{\mathbf{y}}_P$.

A. Conventional VLC CE techniques

The LS CE problem may be formulated as

$$\widehat{\mathbf{h}}_{\text{LS}} = \arg\min_{\mathbf{h}} ||\overline{\mathbf{y}}_P - \mathbf{B}\mathbf{h}||_2^2. \quad (23)$$

Differentiating the cost function of (23) with respect to the CIR vector $\mathbf{h}$ and setting it to zero yields:

$$\frac{\partial}{\partial \mathbf{h}}[(\overline{\mathbf{y}}_P - \mathbf{B}\mathbf{h})^H(\overline{\mathbf{y}}_P - \mathbf{B}\mathbf{h})] = \mathbf{0}, \quad (24)$$

where (24) represents the well-known LS solution, which is given as $\widehat{\mathbf{h}}_{\text{LS}} = (\mathbf{B}^H\mathbf{B})^{-1}\mathbf{B}^H\overline{\mathbf{y}}_P$ [53]. The estimated CFR is obtained as $\widehat{\overline{\mathbf{h}}}_{\text{LS}} = \mathbf{Q}\widehat{\mathbf{h}}_{\text{LS}}$. Although the LS approach has a low computational complexity, it is prone to noise under low-SNR conditions [13].

By contrast, the LMMSE estimator minimizes the mean square error (MSE) of the channel estimate, which relies on a linear estimator defined as $\widehat{\mathbf{h}}_{\text{LMMSE}} = \mathbf{L}\overline{\mathbf{y}}_P$. The MSE is characterized by $\mathbb{E}\left[||\widehat{\mathbf{h}}_{\text{LMMSE}} - \mathbf{h})||_2^2\right]$. Minimizing the MSE with respect to $\mathbf{L}$ results in $\mathbf{L} = \mathbf{R}_{\mathbf{h}\overline{\mathbf{y}}_P}\mathbf{R}^{-1}_{\overline{\mathbf{y}}_P\overline{\mathbf{y}}_P}$. Thus, the LMMSE estimator of the multipath CIR $\mathbf{h}$ is given by

$$\widehat{\mathbf{h}}_{\text{LMMSE}} = \mathbf{R}_{\mathbf{h}\overline{\mathbf{y}}_P}\mathbf{R}^{-1}_{\overline{\mathbf{y}}_P\overline{\mathbf{y}}_P}\overline{\mathbf{y}}_P, \quad (25)$$

where $\mathbf{R}_{\mathbf{h}\overline{\mathbf{y}}_P} = \mathbb{E}[\mathbf{h}\overline{\mathbf{y}}_P^H]$ and $\mathbf{R}_{\overline{\mathbf{y}}_P\overline{\mathbf{y}}_P} = \mathbb{E}[\overline{\mathbf{y}}_P\overline{\mathbf{y}}_P^H]$ are the cross-covariance between the CIR $\mathbf{h}$ and the pilot output $\overline{\mathbf{y}}_P$, and auto-covariance of $\overline{\mathbf{y}}_P$, respectively. Substituting the expressions for the above quantities into (25), the estimator can be reduced to [53]

$$\widehat{\mathbf{h}}_{\text{LMMSE}} = (\mathbf{B}^H\mathbf{R}_w^{-1}\mathbf{B} + \mathbf{R}_{\mathbf{hh}}^{-1})^{-1}\mathbf{B}^H\mathbf{R}_w\overline{\mathbf{y}}_P, \quad (26)$$

where $\mathbf{R}_{\mathbf{hh}} = \mathbb{E}[\mathbf{h}\mathbf{h}^H]$ denotes the *a priori* covariance matrix of the CIR vector $\mathbf{h}$ and $\mathbf{R}_w = \mathbb{E}[\overline{\mathbf{w}}_P\overline{\mathbf{w}}_P^H]$ denotes the noise covariance matrix [53].

We note however that these conventional CE techniques do not exploit the sparsity of the CIR $\mathbf{h}$. Furthermore, these schemes require the number of pilots to satisfy $M_P \geq L_h$, for having a reliable estimate, which can lead to a substantial pilot overhead. To avoid this, one can beneficially leverage the sparsity of the multipath scattering VLC channel using sparse signal reconstruction approaches, which are eminently suitable for the CE problem in (22). In this context, the modified l_0-norm minimization-based sparse CE problem constructed for noisy observations can be formulated as shown below

$$\begin{aligned} &\underset{\mathbf{h}}{\text{minimize}} \quad \|\mathbf{h}\|_0 \\ &\text{subject to} \quad \|\overline{\mathbf{y}}_P - \mathbf{B}\mathbf{h}\|_2^2 \leq \xi, \end{aligned} \quad (27)$$

where ξ is a suitably chosen threshold. Typically, since ξ depends on the noise power, it is set as $\xi = \text{Tr}\,(\mathbf{R}_w)$, where $\mathbf{R}_w = \mathbb{E}[\overline{\mathbf{w}}_P\overline{\mathbf{w}}_P^H]$ denotes the noise covariance matrix. A prominent advantage of the sparse signal recovery based problem formulation above is that one can readily recover the sparse vector $\mathbf{h}$ by relying on a reduced number of observations in the vector $\overline{\mathbf{y}}_P$, thanks to the advances in sparse signal recovery [54], [55]. The next section describes an OMP-based algorithm conceived for efficiently solving the above sparse reconstruction problem using a low number of measurements, i.e., $M_P << L_h$.

B. OMP-based sparse VLC CIR estimation

The OMP algorithm is a canonical greedy iterative algorithm designed for sparse approximation [56], which finds the atom, i.e., a column of the measurement matrix $\mathbf{B}$ in each iteration, that is best aligned with the current residual measurement vector. In its successive iterations, the OMP specifically chooses an atom for ensuring that the residual error is orthogonal to the previously picked atoms. This process continues until a suitable termination criterion is satisfied. The process of sparse CE relying on OMP is shown in Algorithm 1. The primary steps of this method can be summarized as follows. For every iteration t, Step-3 evaluates the column index $\mathcal{J}$ of the measurement matrix $\mathbf{B}$ that has the maximum correlation with the residue vector $\mathbf{r}_{t-1}$. The index set Υ_t is updated in Step-4. In Step-5, the matrix $\mathbf{B}^{\Upsilon}$ is augmented by incorporating the $\mathcal{J}^{\text{th}}$ column of the measurement matrix $\mathbf{B}$. Step-6 yields the LS solution $\mathbf{h}_t$ and Step-7 updates the residue $\mathbf{r}_t$, respectively. This process terminates once the difference between the l_2-norm

Algorithm 1: OMP-based sparse VLC CIR estimation

Input: Measurement matrix $\mathbf{B}$, observation vector $\overline{\mathbf{y}}_P$, stopping parameter Ξ

Output: Estimated CIR $\mathbf{h}$

Initialization: Index set Υ_0 = [], residue $\mathbf{r}_{-1} = \mathbf{0}$, $\mathbf{r}_0 = \overline{\mathbf{y}}_P$, iteration number $t = 1$, $\mathbf{B}^{\Upsilon}$ =[], $\widehat{\mathbf{h}}_{\text{OMP}} = \mathbf{0}$

while $(\mid ||\mathbf{r}_{t-1}||_2^2 - ||\mathbf{r}_{t-2}||_2^2 \mid \geq \Xi)$ **do**

$\mathcal{J} = \underset{k=1,2,\ldots,L_h}{\arg\max} \; |\mathbf{B}(:,k)^H \mathbf{r}_{t-1}|$

$\Upsilon_t = \Upsilon_{t-1} \cup \mathcal{J}$

$\mathbf{B}^{\Upsilon} = [\mathbf{B}^{\Upsilon} \;\; \mathbf{B}(:,\mathcal{J})]$

$\mathbf{h}_t = (\mathbf{B}^{\Upsilon})^{\dagger} \overline{\mathbf{y}}_P$

$\mathbf{r}_t = \overline{\mathbf{y}}_P - \mathbf{B}^{\Upsilon} \mathbf{h}_t$

t = t + 1

end

return: $\widehat{\mathbf{h}}_{\text{OMP}}(\Upsilon_t) = \mathbf{h}_t$

of successive residues falls below a specified threshold Ξ, as described in Step-2. Finally, the non-zero locations of the OMP-based estimate $\widehat{\mathbf{h}}_{\text{OMP}}$ are assigned the corresponding coefficients of the LS estimate $\mathbf{h}_t$ obtained in the last iteration, as per the column indices of the measurement matrix chosen in the various iterations. Although OMP is a popular low-complexity sparse signal recovery technique, it suffers from several drawbacks. To begin with, its performance is sensitive to both the stopping criterion employed as well as to the choice of the measurement matrix $\mathbf{B}$. Furthermore, the iterative process may also lead to errors that propagate to the final solution [38], [39], [57].

Another competing sparse signal reconstruction technique is the FOCUSS, whose performance is sensitive to the regularisation parameter and has a propensity to converge to suboptimal local minima, resulting in convergence deficiencies [38], [39], [57]. To overcome these drawbacks of OMP and FOCUSS, we propose a BL-based sparse signal recovery method, which is free of regularization/tuning and exhibits robust convergence [57].

V. Bayesian Learning (BL)-Aided Sparse CSI Estimation in VLC systems

This section outlines the BL technique proposed for the estimation of the sparse VLC CIR $\mathbf{h}$ using the received pilot vector $\overline{\mathbf{y}}_P$. The BL technique proposed begins by assigning a parameterized Gaussian prior $f(\mathbf{h};\mathbf{\Gamma})$ to the unknown sparse VLC CIR vector $\mathbf{h} \in \mathbb{R}^{L_h \times 1}$ as follows [57]

$$f(\mathbf{h};\mathbf{\Gamma}) = \prod_{k=1}^{L_h} (2\pi\gamma_k)^{-\frac{1}{2}} \exp\left(-\frac{|h(k)|^2}{2\gamma_k}\right), \tag{28}$$

where $\mathbf{\Gamma} = \text{diag}(\gamma_1, \gamma_2, \ldots, \gamma_{L_h}) \in \mathbb{R}_+^{L_h \times L_h}$ is the hyperparameter matrix and γ_k is the hyperparameter, which denotes the prior variance of the kth component of $\mathbf{h}$. From the initial assignment of the prior above, it can be seen that when the hyperparameter obeys $\gamma_k \to 0$, the corresponding channel component $h(k) \to 0$ [57]. Therefore, estimating the VLC channel vector $\mathbf{h}$ is equivalent to estimating the associated hyperparameter vector $\boldsymbol{\gamma} = [\gamma_1, \gamma_2, \ldots, \gamma_{L_h}]^T$. Note that the hyperparameters γ_k are unknown and the proposed BL procedure estimates them by maximizing the Bayesian evidence $f(\overline{\mathbf{y}}_P;\mathbf{\Gamma})$. Toward this, consider the likelihood function $f(\overline{\mathbf{y}}_P|\mathbf{h})$ shown below, which follows from $\overline{\mathbf{w}}_P \sim \mathcal{CN}(\mathbf{0}, \mathbf{R}_w)$:

$$\begin{aligned} f(\overline{\mathbf{y}}_P|\mathbf{h}) &= (\pi)^{-M_P} |\mathbf{R}_w|^{-1} \\ &\quad \times \exp\left(-(\overline{\mathbf{y}}_P - \mathbf{B}\mathbf{h})^H \mathbf{R}_w^{-1} (\overline{\mathbf{y}}_P - \mathbf{B}\mathbf{h})\right). \end{aligned} \tag{29}$$

Thus, the Bayesian evidence is given by

$$\begin{aligned} f(\overline{\mathbf{y}}_P;\mathbf{\Gamma}) &= \int f(\overline{\mathbf{y}}_P|\mathbf{h}) f(\mathbf{h};\mathbf{\Gamma}) d\mathbf{h} \\ &= (\pi)^{-M_P} (\det(\mathbf{\Sigma}_{\overline{\mathbf{y}}_P}))^{-1} \exp\left(-\overline{\mathbf{y}}_P^H \mathbf{\Sigma}_{\overline{\mathbf{y}}_P}^{-1} \overline{\mathbf{y}}_P\right), \end{aligned} \tag{30}$$

where $\mathbf{\Sigma}_{\overline{\mathbf{y}}_P} = \mathbf{R}_w + \mathbf{B}\mathbf{\Gamma}\mathbf{B}^H \in \mathbb{C}^{M_P \times M_P}$ is the covariance matrix of the output pilot vector $\overline{\mathbf{y}}_P$. The optimization objective formulated for determining the maximum-likelihood (ML) estimate of the hyperparameter vector $\boldsymbol{\gamma}$ is given by

$$\log f(\overline{\mathbf{y}}_P;\mathbf{\Gamma}) = -M_P \log(\pi) - \log\left(\det\left(\mathbf{\Sigma}_{\overline{\mathbf{y}}_P}\right)\right) - \overline{\mathbf{y}}_P^H \mathbf{\Sigma}_{\overline{\mathbf{y}}_P}^{-1} \overline{\mathbf{y}}_P. \tag{31}$$

Observe that the direct maximization of $\log f(\overline{\mathbf{y}}_P;\mathbf{\Gamma})$ is intractable, since it has multiple local maxima, which renders it non-concave. In the face of this impediment, the EM algorithm may be harnessed for the iterative maximization of $\log f(\overline{\mathbf{y}}_P;\mathbf{\Gamma})$. In each iteration, the optimization objective increases due to the properties of the EM method, which ensure that the log-likelihood metric converges to a fixed point. Consequently, the robust convergence of the EM technique and the unique prior assignment $f(\mathbf{h};\mathbf{\Gamma})$ of the proposed BL result in beneficial performance enhancement for the sparse CIR estimator of VLC systems. The EM steps of hyperparameter estimation are derived next.

Let $\widehat{\gamma}_k^{(m)}$ represent the kth hyperparameter estimate calculated in the mth iteration, and the associated hyperparameter matrix be $\widehat{\mathbf{\Gamma}}^{(m)} = \text{diag}(\widehat{\gamma}_k^{(1)}, \widehat{\gamma}_k^{(2)}, \ldots, \widehat{\gamma}_k^{(L_h)})$. The expectation step (E-step) uses the complete dataset $\{\overline{\mathbf{y}}_P, \mathbf{h}\}$ in the mth iteration for computing the log-likelihood $\mathcal{L}(\mathbf{\Gamma}|\widehat{\mathbf{\Gamma}}^{(m)})$ as follows

$$\begin{aligned} \mathcal{L}(\mathbf{\Gamma}|\widehat{\mathbf{\Gamma}}^{(m)}) &= \mathbb{E}_{\mathbf{h}|\overline{\mathbf{y}}_P;\widehat{\mathbf{\Gamma}}^{(m)}} \Big\{ \log f(\overline{\mathbf{y}}_P, \mathbf{h};\mathbf{\Gamma}) \Big\} \\ &= \mathbb{E}_{\mathbf{h}|\overline{\mathbf{y}}_P;\widehat{\mathbf{\Gamma}}^{(m)}} \Big\{ \log f(\overline{\mathbf{y}}_P|\mathbf{h}) + \log f(\mathbf{h};\mathbf{\Gamma}) \Big\}. \end{aligned} \tag{32}$$

One can observe from (29) that the likelihood $f(\overline{\mathbf{y}}_P|\mathbf{h})$ is independent of the hyperparameter matrix $\mathbf{\Gamma}$. Hence, one can ignore the first term of (32) in the following maximization step (M-step). Next, the M-step updates the hyperparameter vector $\widehat{\boldsymbol{\gamma}}^{m+1}$ by maximizing the above optimization objective with respect to $\boldsymbol{\gamma}$ as

$$\widehat{\boldsymbol{\gamma}}^{(m+1)} = \arg\max_{\boldsymbol{\gamma}} \mathbb{E}_{\mathbf{h}|\overline{\mathbf{y}}_P;\widehat{\mathbf{\Gamma}}^{(m)}} \Big\{ \log f(\mathbf{h};\mathbf{\Gamma}) \Big\}$$

Algorithm 2: BL-based sparse VLC CIR estimation

Input: Received pilot vector $\overline{\mathbf{y}}_P \in \mathbb{C}^{M_P \times 1}$, measurement matrix $\mathbf{B} \in \mathbb{C}^{M_P \times L_h}$, noise covariance matrix $\mathbf{R}_w$, stopping parameters ϵ and $m_{\max}$

Output: Estimated CIR $\mathbf{h}$

Initialization:

$\widehat{\gamma}_k^{(0)} = 1,\ \forall 1 \leq k \leq L_h \Longrightarrow \widehat{\mathbf{\Gamma}}^{(0)} = \mathbf{I}_{L_h}$ Initialize counter $m = -1$ and $\widehat{\mathbf{\Gamma}}^{(-1)} = \mathbf{0}$

while $(\parallel \widehat{\boldsymbol{\gamma}}^{(m+1)} - \widehat{\boldsymbol{\gamma}}^{(m)} \parallel_2 > \epsilon \ \ \&\& \ \ m < m_{\max})$ **do**

  $m \leftarrow m + 1$

  E Step: Compute the *a posteriori* covariance and mean as

  $\mathbf{\Sigma}_{\mathbf{h}}^{(m)} = \left(\mathbf{B}^H \mathbf{R}_w^{-1} \mathbf{B} + \left(\widehat{\mathbf{\Gamma}}^{(m)}\right)^{-1}\right)^{-1}$

  $\boldsymbol{\mu}_{\mathbf{h}}^{(m)} = \mathbf{\Sigma}_{\mathbf{h}}^{(m)} \mathbf{B}^H \mathbf{R}_w^{-1} \overline{\mathbf{y}}_P$

  M Step: Update the estimates of the hyperparameters as

  for $k = 0, 1, 2, \ldots, L_h$ **do**

    $\widehat{\gamma}_k^{(m+1)} = \mathbf{\Sigma}_{\mathbf{h}}^{(m)}(k,k) + |\boldsymbol{\mu}_{\mathbf{h}}^{(m)}(k)|^2$

  end

end

return: $\widehat{\mathbf{h}}_{\text{BL}} = \boldsymbol{\mu}_{\mathbf{h}}^{(m)}$

$$= \arg\max_{\boldsymbol{\gamma}} \sum_{k=1}^{L_h} \left(- \frac{\log(2\pi\gamma_k)}{2} - \frac{\mathbb{E}_{\mathbf{h}|\overline{\mathbf{y}}_P;\widehat{\mathbf{\Gamma}}^{(m)}} \left\{ |\mathrm{h}(k)|^2 \right\}}{2\gamma_k} \right). \tag{33}$$

From (33) above, it can be observed that the maximization problem can be decomposed into L_h distinct maximization problems related to the particular hyperparameters γ_k as follows

$$\widehat{\gamma}_k^{(m+1)} = \arg\max_{\gamma_k} \left(- \frac{\log(2\pi\gamma_k)}{2} - \frac{\mathbb{E}_{\mathbf{h}|\overline{\mathbf{y}}_P;\widehat{\mathbf{\Gamma}}^{(m)}} \left\{ |\mathrm{h}(k)|^2 \right\}}{2\gamma_k} \right). \tag{34}$$

Upon differentiating (34) with respect to γ_k and setting it to zero, the estimate of the hyperparameter γ_k can be obtained as

$$\widehat{\gamma}_k^{(m+1)} = \mathbb{E}_{\mathbf{h}|\overline{\mathbf{y}}_P;\widehat{\mathbf{\Gamma}}^{(m)}} \left\{ |\mathrm{h}(k)|^2 \right\} = |\boldsymbol{\mu}_{\mathbf{h}}^{(m)}(k)|^2 + \mathbf{\Sigma}_{\mathbf{h}}^{(m)}(k,k). \tag{35}$$

In the above, the last step follows from the *a posteriori* probability density function of $\mathbf{h}$ given as $f(\mathbf{h}|\overline{\mathbf{y}}_P; \widehat{\mathbf{\Gamma}}^{(m)}) \sim \mathcal{CN}\left(\boldsymbol{\mu}_{\mathbf{h}}^{(m)}, \mathbf{\Sigma}_{\mathbf{h}}^{(m)}\right)$ [58], where the $\boldsymbol{\mu}_{\mathbf{h}}^{(m)} = \mathbf{\Sigma}_{\mathbf{h}}^{(m)} \mathbf{B}^H \mathbf{R}_w^{-1} \overline{\mathbf{y}}_P \in \mathbb{C}^{L_h \times 1}$ is the mean and $\mathbf{\Sigma}_{\mathbf{h}}^{(m)} = \left(\mathbf{B}^H \mathbf{R}_w^{-1} \mathbf{B} + \left(\widehat{\mathbf{\Gamma}}^{(m)}\right)^{-1}\right)^{-1} \in \mathbb{C}^{L_h \times L_h}$ is the corresponding covariance matrix. Therefore, the BL-based sparse CSI estimate of the VLC channel upon convergence is computed as $\widehat{\mathbf{h}}_{\text{BL}} = \boldsymbol{\mu}_{\mathbf{h}}^{(m)}$. Algorithm 2 summarizes the steps involved in the proposed BL-aided sparse CSI estimation.

According to [57], the BL-based log-likelihood function demonstrates fewer local maxima compared to the schemes like FOCUSS [59], which enables the BL to converge to the global minima, leading to its improved convergence properties. Furthermore, the EM algorithm in BL guarantees global convergence to a fixed log-likelihood point, with the optimization objective increasing in each iteration. Regarding convergence speed, recent research [60] demonstrates that when approximating the parameters of a two-component Gaussian mixture model, the EM algorithm typically converges rapidly, within only 10 iterations. Consequently, the proposed BL-based method is expected to perform well even in a time-varying VLC channel since it converges very fast, typically within $5-10$ iterations. Therefore, combining the robust convergence of the EM algorithm with the properties of the BL-based log-likelihood yields improved performance for sparse CE. The subsequent section presents our performance benchmarks, which include the O-MMSE estimator and the BCRLB.

A. BCRLB and O-MMSE

We now derive various performance benchmarks for the proposed estimation scheme. The BCRLB harnessed for benchmarking the MSE of the estimated CSI $\widehat{\mathbf{h}}$ is derived as follows. The Bayesian Fisher Information Matrix (BFIM) $\mathbf{J}_B \in \mathbb{C}^{L_h \times L_h}$ of the VLC CIR $\mathbf{h} \in \mathbb{R}^{L_h \times 1}$ is obtained as [61]

$$\mathbf{J}_B = \mathbf{J}_P + \mathbf{J}_D. \tag{36}$$

The quantity $\mathbf{J}_D$ in the above expression is the FIM associated with the pilot output $\overline{\mathbf{y}}_P$, which is termed as the expected information matrix expressed as $\mathbf{J}_D = -\mathbb{E}_{\overline{\mathbf{y}}_P,\mathbf{h}} \left\{ \frac{\partial^2 \mathcal{L}(\overline{\mathbf{y}}_P|\mathbf{h})}{\partial \mathbf{h} \partial \mathbf{h}^H} \right\}$. Furthermore, $\mathbf{J}_P$ is the FIM associated with the CSI $\mathbf{h}$, which is termed the prior information matrix expressed as $\mathbf{J}_P = -\mathbb{E}_{\mathbf{h}} \left\{ \frac{\partial^2 \mathcal{L}(\mathbf{h};\mathbf{\Gamma})}{\partial \mathbf{h} \partial \mathbf{h}^H} \right\}$ [61]. The quantity $\mathcal{L}(\overline{\mathbf{y}}_P|\mathbf{h}) = \log f(\overline{\mathbf{y}}_P|\mathbf{h})$ and $\mathcal{L}(\mathbf{h};\mathbf{\Gamma}) = \log f(\mathbf{h};\mathbf{\Gamma})$ represents the log-likelihood corresponding to the received pilot vector $\overline{\mathbf{y}}_P$ and log-prior density of the VLC channel vector $\mathbf{h}$, respectively, which are expressed as

$$\begin{aligned} \mathcal{L}(\overline{\mathbf{y}}_P|\mathbf{h}) &= C_1 - (\overline{\mathbf{y}}_P - \mathbf{B}\mathbf{h})^H \mathbf{R}_w^{-1} (\overline{\mathbf{y}}_P - \mathbf{B}\mathbf{h}) \\ &= C_1 - \overline{\mathbf{y}}_P^H \mathbf{R}_w^{-1} \overline{\mathbf{y}}_P + \mathbf{h}^H \mathbf{B}^H \mathbf{R}_w^{-1} \overline{\mathbf{y}}_P \\ &\quad + \overline{\mathbf{y}}_P^H \mathbf{R}_w^{-1} \mathbf{B}\mathbf{h} - \mathbf{h}^H \mathbf{B}^H \mathbf{R}_w^{-1} \mathbf{B}\mathbf{h} \end{aligned} \tag{37}$$

$$\mathcal{L}(\mathbf{h};\Gamma) = C_2 - \mathbf{h}^H (\mathbf{\Gamma})^{-1} \mathbf{h}, \tag{38}$$

where $C_1 = -M_P \log(\pi) - \log[\det(\mathbf{R}_w)]$ and $C_2 = -\log[\det(\mathbf{\Gamma})] - L_h \log(\pi)$ are the constants, independent of $\mathbf{h}$. Here $\mathbf{\Gamma}$ denotes the true hyperparameter matrix that is obtained using the known parameter delay profile. Upon substituting the above quantities into $\mathbf{J}_D$ and $\mathbf{J}_P$ of (36), and rearranging the resultant expressions further, the FIMs $\mathbf{J}_D$ and $\mathbf{J}_P$ can be formulated as $\mathbf{J}_D = \mathbf{B}^H \mathbf{R}_w^{-1} \mathbf{B}$ and $\mathbf{J}_P = \mathbf{\Gamma}^{-1}$. Thus, the Bayesian FIM $\mathbf{J}_B$ can

TABLE 2: **Simulation parameters for the VLC system**

Parameter	Value	Parameter	Value
Room Dimension	5 m × 5 m × 3 m	Transmitter Location	$(2.5, 2.5, 3)$
Reflection Coefficient (ρ)	0.8	Transmit power of each LED (P_S)	20 mW
Number of LEDs in each array (N_{LED})	60 × 60 (3600)	Azimuth angle	0°
Semi-half power angle ($\phi_{1/2}$)	70°	FoV (Ψ_{FoV})	60°
PD responsivity (R_{PD})	1	Detector area (A_{R_b})	1 cm^2
Elevation angle	90°	Height of receiver plane from the floor	0.85 m
Refractive index of lens (μ)	1.5	Modulation	DCO-OFDM, ACO-OFDM
DC Bias	7 dB	Constellation	4-QAM
No. of subcarriers (N)	1024	CP length (N_{CP})	256
Smallest FD pilot subcarrier index (I_0)	2	Outage Capacity (C_ζ)	8 bps/Hz
Distribution of pilots	Comb type	CIR order (L_h)	40
No. of dominant paths	6	FD pilot interval (I_P)	40

be expressed as $\mathbf{J}_B = \mathbf{B}^H\mathbf{R}_w^{-1}\mathbf{B} + \mathbf{\Gamma}^{-1}$. Therefore, the BCRLB for the MSE of the sparse VLC CIR estimate $\widehat{\mathbf{h}}$, defined as $\text{MSE} = \mathbb{E}\left[||\mathbf{h} - \widehat{\mathbf{h}}||_2^2\right]$ becomes:

$$\text{MSE}\left(\widehat{\mathbf{h}}\right) \geq \text{Tr}\left(\mathbf{J}_B^{-1}\right) = \text{Tr}\left(\left[\mathbf{B}^H\mathbf{R}_w^{-1}\mathbf{B} + \mathbf{\Gamma}^{-1}\right]^{-1}\right). \tag{39}$$

We also derive the O-MMSE estimator considering perfect knowledge of the parameter delay profile of the VLC channel. Based on the parameter delay profile, let the support-set $\mathcal{S}$ represent the locations of the non-zero indices of the sparse multipath VLC channel and $\mathbf{B}_{\text{O}} = \mathbf{B}(:, \mathcal{S})$ denote the oracle-sensing matrix, which is constructed of the columns of $\mathbf{B}$ indexed by $\mathcal{S}$. The O-MMSE estimate is then obtained as

$$\widehat{\mathbf{h}}_{\text{O-MMSE}} = \left(\mathbf{B}_{\text{O}}^H\mathbf{R}_w^{-1}\mathbf{B}_{\text{O}} + \mathbf{I}_{L_h}^{-1}\right)^{-1}\mathbf{B}_{\text{O}}^H\mathbf{R}_w^{-1}\overline{\mathbf{y}}_P. \tag{40}$$

B. Computational Complexity Analysis

In this subsection, we discuss the complexity of the CE techniques developed in our work. The computational complexity of our BL-based sparse CE technique is of the order $\mathcal{O}\left(L_h^3\right)$ due to the matrix inversion of size $L_h \times L_h$. By contrast, the complexity order for the worst-case scenario of the OMP algorithm is $\mathcal{O}\left(M_P^3\right)$, as a result of the intermediate LS estimate required at each iteration. The traditional LMMSE-based CE technique has a computational complexity of the order $\mathcal{O}\left(L_h^3\right)$. The performance of the proposed BL-based approach is compared to that of other conventional approaches in the following section.

VI. Simulation Results

This section outlines our simulation results to illustrate and compare the performance of the proposed BL-based scheme to that of the FOCUSS and OMP-based [5], [25] sparse signal recovery schemes in addition to the traditional LS [5] and LMMSE [13] CIR estimators of a multipath O-OFDM VLC system in the context of the BER, OP, and NMSE metrics. The BER characterizes the detection performance attained by the receivers constructed using the CSI estimates gleaned. The OP is defined as the probability that the maximum achievable rate is below the outage capacity threshold C_ζ, i.e., $Pr(\log_2(1 + \text{SNR}) \leq C_\zeta) = \zeta$ [62], [63]. In our simulations, $\mathbf{R}_w = \sigma^2_{\text{AWGN}}\mathbf{I}_{M_P}$, $\mathbf{R}_{\mathbf{hh}} = \mathbf{I}_{L_h}$, and the SNR in decibels (dB) is described as the SNR (dB) = $10\log_{10}\left(\frac{P_{\overline{x}}}{\sigma^2_{\text{AWGN}}}\right)$. Finally, the NMSE is defined as $\text{NMSE} = \frac{||\widehat{\mathbf{h}}-\mathbf{h}||_2^2}{||\mathbf{h}||_2^2}$. The stopping criteria for the BL are set as $\epsilon = 10^{-6}$ and $m_{\max} = 50$, whereas that of the OMP is set to $\Xi = 0.1$. The regularization parameter for the competing FOCUSS is set as the noise variance σ^2_{AWGN}, the l_p-norm parameter is set to $p = 0.8$ with a stopping threshold of 10^{-5}, and the maximum number of iterations is set to 800. The simulation parameters used are given in Table 2, unless stated otherwise, which are based on the real environmental conditions mentioned in [7], [13], [18], [23], [27]–[29], [44].

Figure 6a shows the proposed BL-based technique's NMSE performance along with that of the other techniques for our DCO-OFDM system. It is apparent that the proposed BL-based approach performs better than the competing techniques. Since the traditional LS and LMMSE techniques do not leverage the sparsity of the multipath CIR of the VLC system, their NMSE performance is inferior. The OMP, although exploits sparsity, performs poorly, because it is sensitive to both the dictionary matrix chosen and to the stopping parameter, which is set to $\Xi = 0.1$, while the dismal performance of FOCUSS is due to its inability to converge and its dependence on the regularization parameter [25], [38], [57]. By contrast, our BL-based sparse estimation method efficiently exploits sparsity via EM-based hyperparameter estimation, which does not require any tuning/regularization parameter and has robust convergence. As a further benefit, the proposed BL-based approach is insensitive to the choice of the dictionary matrix. Furthermore, the NMSE performance is also compared with respect to the BCRLB and O-MMSE of (39) and (40) respectively, which have also been suitably normalized by $||\mathbf{h}||_2^2$. As a result, the proposed BL

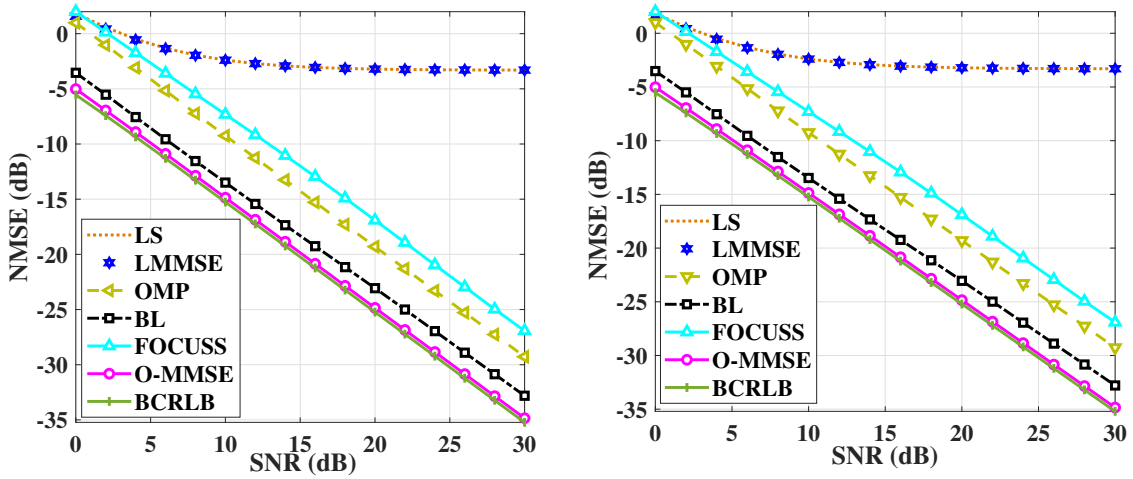

FIGURE 6: NMSE versus SNR performance of the VLC system with $M_P = 16$, $L_h = 40$, and 4 QAM modulation (a) DCO-OFDM; (b) ACO-OFDM.

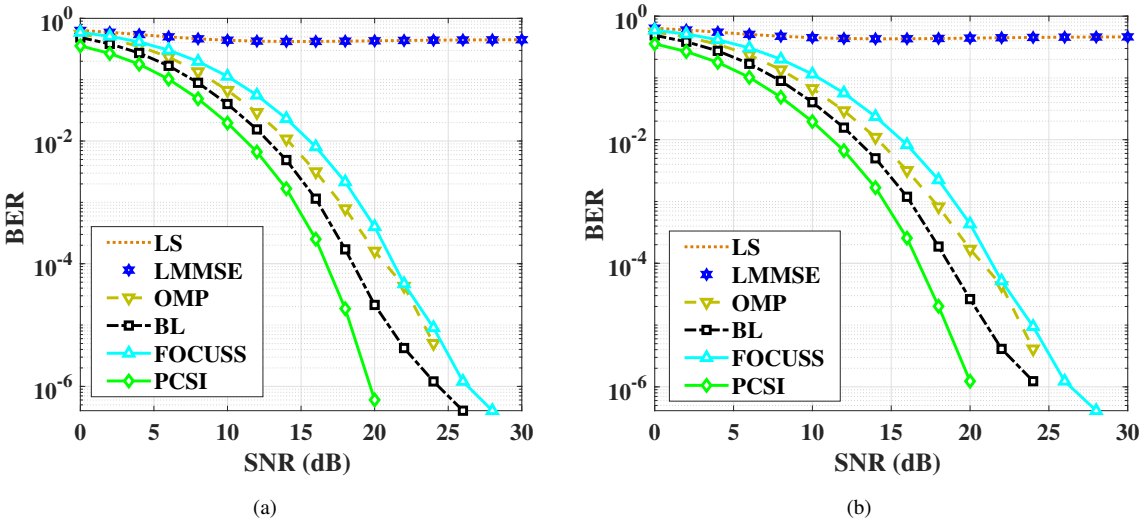

FIGURE 7: BER versus SNR performance of the VLC system with $M_P = 16$, $L_h = 40$, and 4 QAM modulation (a) DCO-OFDM; (b) ACO-OFDM.

method yields an NMSE that is closer to the corresponding O-MMSE and BCRLB derived. The NMSE performance of the different estimation strategies harnessed for our ACO-OFDM system is compared in Figure 6b. A similar pattern has been seen here as well, with the BL technique yielding the superior result overall. Figure 7a and Figure 7b illustrate the BER of all the competing systems for DCO and ACO-OFDM modulation. As illustrated in Figure 7, the BER attained by our BL-based CE is significantly lower than that of its OMP and FOCUSS counterparts due to its enhanced estimation accuracy. In addition, the proposed BL-based BER performance is seek to approach the BER of a receiver using perfect CSI (PCSI), demonstrating their significantly improved potential for high-integrity signal recovery.

Figure 8a compares the BER performance of the BL-based technique conceived to that of the OMP technique for $4, 16, 64,$ and 256 level QAM for our DCO-OFDM system. It is apparent that the proposed BL-based method outperforms the OMP technique for various modulation orders. A similar BER performance is also observed for the ACO-OFDM, as illustrated in Figure 8b.

Notably, the BL-based framework proposed for CSI estimation transmits M_P pilot symbols in an OFDM block of N symbols. As a result, the normalized pilot overhead is given by $\rho = \frac{M_P}{N}$. Figure 9a and Figure 9b demonstrate the

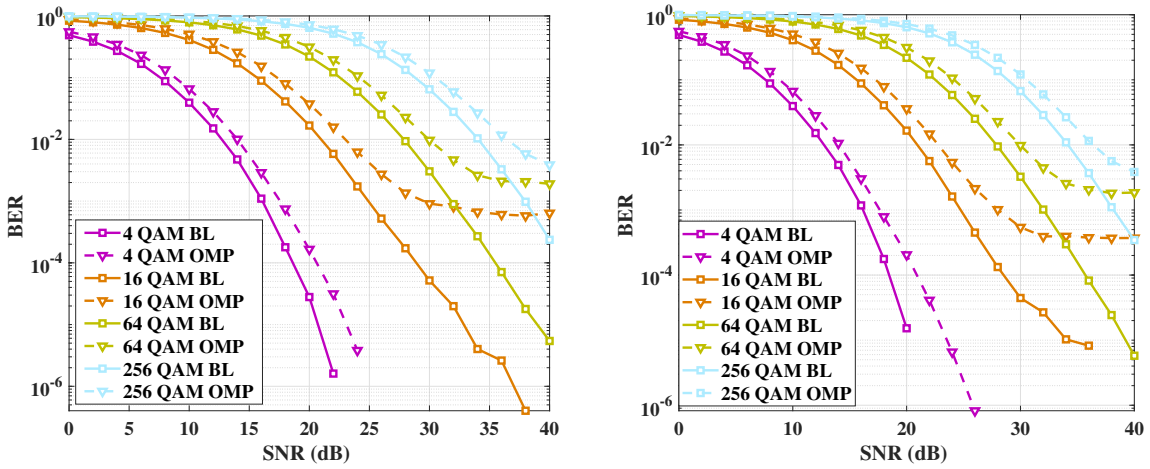

(a) (b)

FIGURE 8: BER versus SNR performance of the VLC system with $M_P = 16$, $L_h = 40$ (a) DCO-OFDM; (b) ACO-OFDM.

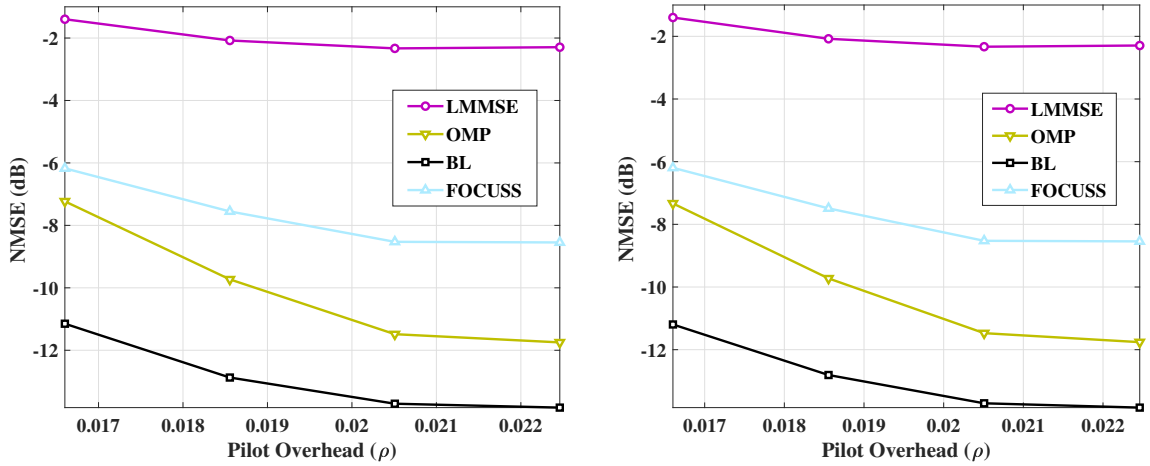

(a) (b)

FIGURE 9: NMSE versus Pilot Overhead (ρ) performance of the VLC system with $M_P = 16$, $L_h = 40$, SNR $= 10$ dB, and 4 QAM modulation (a) DCO-OFDM; (b) ACO-OFDM.

NMSE performance of the DCO and ACO-OFDM systems for different sparse CSI estimation methods upon varying ρ. The SNR for this analysis is set to 10 dB. We observe that increasing the pilot overhead ρ enhances the NMSE performance for all the competing schemes. However, the NMSE of the proposed BL method associated with $\rho = 0.018$ is observed to be lower than that of the OMP with $\rho = 0.022$ in both the O-OFDM systems. This verifies the fact that, for a specified level of NMSE, the BL-based estimation method results in a significant reduction in the ρ, which illustrates its improved bandwidth efficiency.

The OP performance comparison of the suggested BL-based technique and the other contending schemes harnessed for the DCO-OFDM system is depicted in Figure 10a, with the outage capacity, C_ξ set as 8 bps/Hz. Compared to the LS, LMMSE, FOCUSS, and OMP approaches, the OP of the proposed BL method is substantially lower, as demonstrated in Figure 10a. The enhanced OP of the BL approach can naturally be attributed to its enhanced estimation accuracy, when compared to the other CE methods discussed. Figure 10b illustrates the OP of the ACO-OFDM system. Again, the BL-based method outperforms the other sparse CE methods.

Figure 11a depicts the convergence of our proposed BL-based technique as a function of the number of EM iterations for various values of the number of pilot symbols M_P. This represents the number of EM iterations required for the convergence of the hyperparameters. For a fixed value of the convergence parameter $\epsilon = 10^{-6}$, it is evident that the

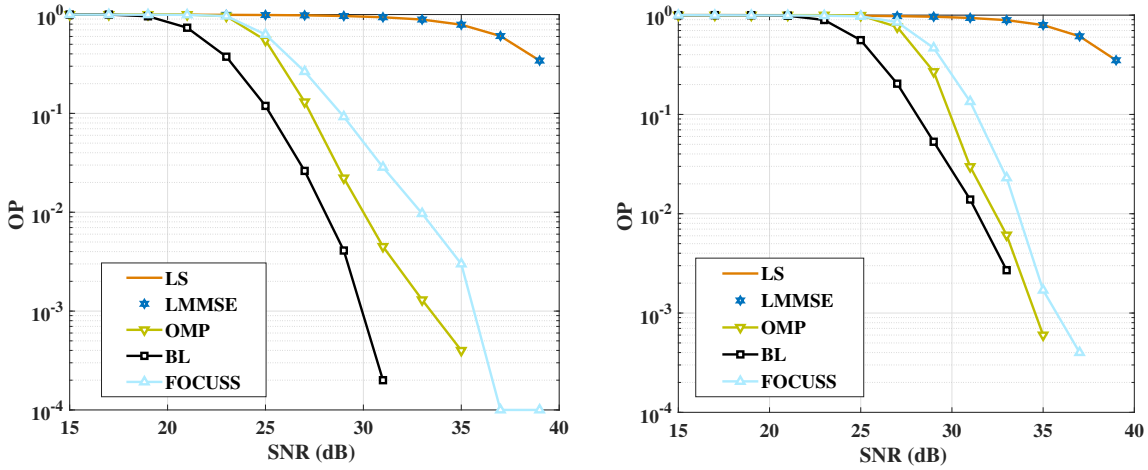

(a) (b)

FIGURE 10: OP versus SNR performance of the VLC system with $M_P = 16$, $L_h = 40$, and 4 QAM modulation (a) DCO-OFDM; (b) ACO-OFDM.

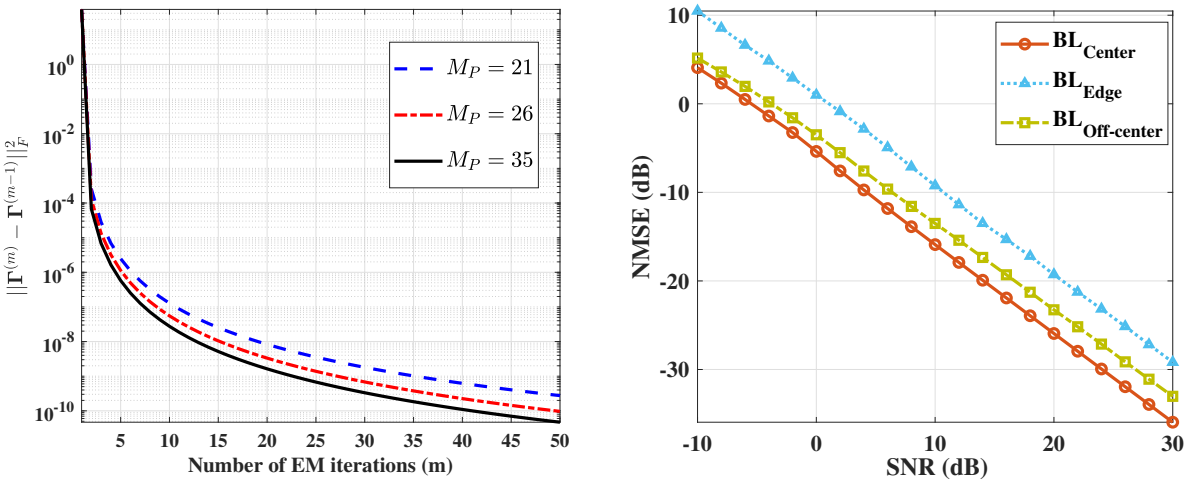

(a) (b)

FIGURE 11: (a) $\left\|\widehat{\mathbf{\Gamma}}^{(m+1)} - \widehat{\mathbf{\Gamma}}^{(m)}\right\|_{\mathrm{F}}^2$ versus number of EM iterations (m) for $N = 1024, L_h = 40$, SNR $= 10$ dB and 4 QAM modulation. (b) NMSE versus SNR performance of the VLC system with $M_P = 16$, $L_h = 40$, and 4 QAM modulation for an LoS path, NLoS paths considering the fifth-order reflections, and LoS with NLoS paths considering the fifth-order reflections in DCO-OFDM.

number of iterations required for convergence decreases as M_P increases.

Figure 11b illustrates the effect of the proposed BL-based CE method on users located in close proximity to the walls of the room as well as those positioned near the center of the room. In the vicinity of the room center, the LoS path plays a dominant role in comparison to the NLoS paths, whereas in the vicinity of the walls, NLoS paths become more significant than the LoS path, as shown in Figure 5. Consequently, in Figure 11b, the "Center" represents the user's location in the center of the room, the "Edge" corresponds to the user's location that is close to the room walls, and the "Off-center" represents the user's location elsewhere within the room. It can be inferred from Figure 11b that, regardless of the user's position within the room, our proposed BL-based method exhibits robust estimation performance in all plausible scenarios.

In order to demonstrate the advantages of the proposed method, we have evaluated the advocated BL-based approach in different simulation environments, where N is 2048, the

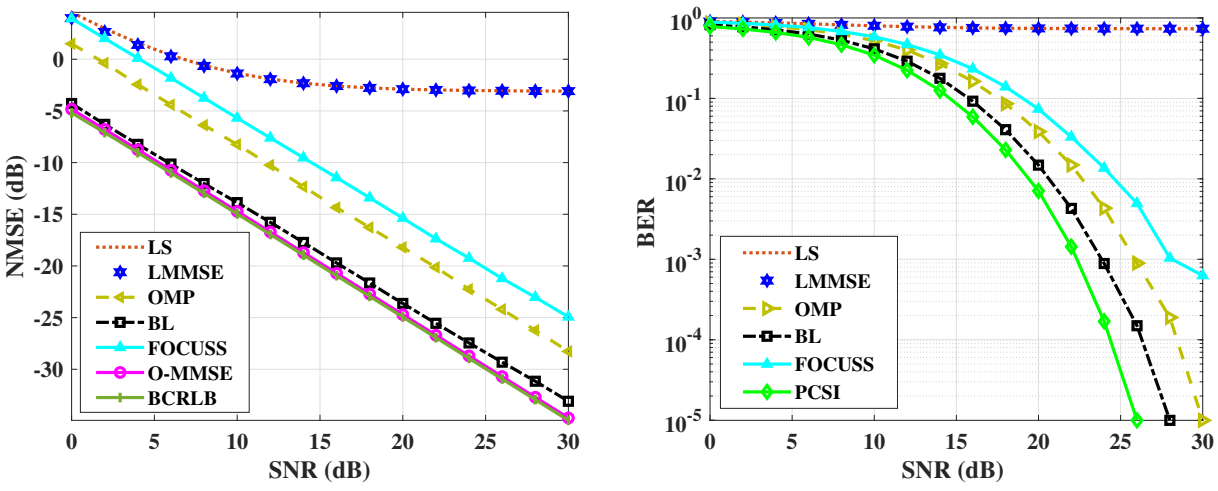

(a) (b)

FIGURE 12: Performance of the CE techniques with proposed BL-based technique for $M_P = 37$ and 16 QAM modulation in DCO-OFDM for (a) NMSE versus SNR; (b) BER versus SNR.

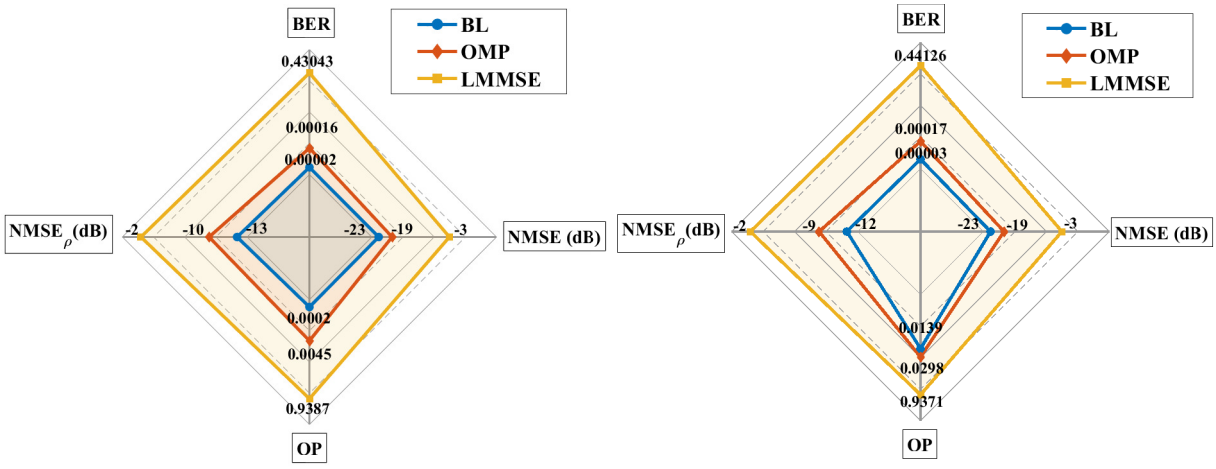

(a) (b)

FIGURE 13: Stylized performance comparison for (a) DCO-OFDM; (b) ACO-OFDM.

no. of dominant paths is 8, the modulation scheme is 16 QAM, I_P is 55, and L_h is 45. Figure 12a compares the variation of NMSE performance to that of other techniques for our DCO-OFDM system. It is evident that the proposed BL-based approach outperforms comparable techniques. Additionally, Figure 12b shows the BER performance. Observe that the BER attained by our BL-based CE technique significantly lower than that of its OMP and FOCUSS counterparts due to its enhanced estimation accuracy and because the BL-based technique seeks to approach the BER of a receiver using PCSI.

Lastly, the comprehensive performance of the proposed BL, OMP, and traditional LMMSE techniques is presented for the DCO-OFDM VLC system in the context of the BER, NMSE, pilot overhead (NMSE$_\rho$), as well as OP in Figure 13a. For this study, the BER and NMSE performance is obtained at SNR = 20 dB, NMSE$_\rho$ is obtained at $\rho = 0.0186$, while the OP performance is obtained at SNR $= 31$ dB. Observe from Figure 13a that for a given SNR, the proposed BL-based approach yields the best OP, NMSE, and BER. Furthermore for a given ρ, the best NMSE is obtained for the BL-based approach. According to the stylized illustration of Figure 13a, the proposed BL-based approach occupies the

smallest area of the quadrilateral, visualizing that it has the lowest BER, OP, NMSE and NMSE$_\rho$ and it is thus the most suitable method for CE in the DCO-OFDM system. A similar comprehensive performance characterization is carried out also for the ACO-OFDM VLC system, as depicted in Figure 13b. We used similar parameters to those of Figure 13a. Once again, the proposed BL-based approach has the smallest area of the quadrilateral, i.e., the best performance. Therefore, the proposed BL-based sparse recovery technique is particularly well suited for implementation in O-OFDM VLC systems as a benefit of its improved CSI estimation, resulting in the best BER and OP, despite its reduced pilot overhead.

VII. Conclusions

A novel BL-based sparse multipath CIR estimation method was designed for IM/DD-based O-OFDM VLC systems. Initially, a sparse multipath CIR model was introduced that comprehensively captured the LoS and NLoS components of the wideband VLC channel. Next, the popular LS and LMMSE CE's were highlighted, which do not leverage the sparsity. These discussions were followed by the OMP, which although exploits the sparsity of the multipath CIR, suffers from poor convergence due to its sensitivity to both the dictionary matrix and to the stopping criterion. To overcome these drawbacks, a novel sparse multipath CIR CE scheme employing the BL framework was developed for O-OFDM VLC systems, which is applicable for both the popular modulation techniques. In comparison to the existing CE techniques, the BL-based CE scheme conceived requires a significantly lower pilot overhead. A closed-form expression was derived for the BCRLB to characterize the best-case MSE of the proposed estimator, thus benchmarking its performance. Our simulation results demonstrated that the BL-based technique outperforms the popular sparse estimation methods like OMP, FOCUSS, as well as the conventional LS and LMMSE in terms of a wide array of metrics, including the MSE, OP, BER, and pilot overhead while achieving a performance close to the bounds. An interesting future direction is to analyze the effect of BL-based CE techniques on the achievable rate of the VLC system.

REFERENCES

[1] W. Jiang, B. Han, M. A. Habibi, and H. D. Schotten, "The road towards 6G: A comprehensive survey," *IEEE Open Journal of the Communications Society*, vol. 2, pp. 334–366, 2021.

[2] S. Mardanikorani, X. Deng, and J.-P. M. Linnartz, "Optimization and comparison of M-PAM and optical OFMD modulation for optical wireless communication," *IEEE Open Journal of the Communications Society*, vol. 1, pp. 1721–1737, 2020.

[3] A. M. Abdelhady, A. K. S. Salem, O. Amin, B. Shihada, and M.-S. Alouini, "Visible light communications via intelligent reflecting surfaces: Metasurfaces vs mirror arrays," *IEEE Open Journal of the Communications Society*, vol. 2, pp. 1–20, 2020.

[4] R. Mesleh, H. Elgala, and H. Haas, "On the performance of different OFDM based optical wireless communication systems," *Journal of Optical Communications and Networking*, vol. 3, no. 8, pp. 620–628, 2011.

[5] P. Miao, G. Chen, X. Wang, Y. Yao, and J. A. Chambers, "Adaptive Nonlinear equalization combining sparse Bayesian learning and Kalman filtering for visible light communications," *Journal of Lightwave Technology*, vol. 38, no. 24, pp. 6732–6745, 2020.

[6] K. Lee, H. Park, and J. R. Barry, "Indoor channel characteristics for visible light communications," *IEEE communications letters*, vol. 15, no. 2, pp. 217–219, 2011.

[7] R. Raj, S. Jaiswal, and A. Dixit, "On the effect of multipath reflections in indoor visible light communication links: Channel characterization and BER analysis," *IEEE Access*, vol. 8, pp. 190 620–190 636, 2020.

[8] J. Barry, J. Kahn, W. Krause, E. Lee, and D. Messerschmitt, "Simulation of multipath impulse response for indoor wireless optical channels," *IEEE Journal on Selected Areas in Communications*, vol. 11, no. 3, pp. 367–379, 1993.

[9] X. Zhang, Z. Babar, P. Petropoulos, H. Haas, and L. Hanzo, "The evolution of optical OFDM," *IEEE communications surveys & tutorials*, vol. 23, no. 3, pp. 1430–1457, 2021.

[10] S. D. Dissanayake and J. Armstrong, "Comparison of ACO-OFDM, DCO-OFDM and ADO-OFDM in IM/DD systems," *Journal of Lightwave Technology*, vol. 31, no. 7, pp. 1063–1072, 2013.

[11] J. Armstrong and A. J. Lowery, "Power efficient optical OFDM," *Electronics letters*, vol. 42, no. 6, pp. 370–372, 2006.

[12] J. M. Kahn and J. R. Barry, "Wireless Infrared Communications," *Proceedings of the IEEE*, vol. 85, no. 2, pp. 265–298, 1997.

[13] H. Zhao, M. Li, R. Wang, and D. Wu, "Channel estimation for asymmetrically clipped optical orthogonal frequency division multiplexing communication system," *Optical Engineering*, vol. 52, no. 7, p. 076111, 2013.

[14] Z. Zhou, C. Chen, and M. Kavehrad, "Impact analyses of high-order light reflections on indoor optical wireless channel model and calibration," *Journal of Lightwave Technology*, vol. 32, no. 10, pp. 2003–2011, 2014.

[15] C. Gong and Z. Xu, "Channel estimation and signal detection for optical wireless scattering communication with inter-symbol interference," *IEEE Transactions on Wireless Communications*, vol. 14, no. 10, pp. 5326–5337, 2015.

[16] X. Qian, H. Deng, and H. He, "Pilot-based parametric channel estimation algorithm for DCO-OFDM-based visual light communications," *Optics Communications*, vol. 400, pp. 150–155, 2017.

[17] P. A. Haigh, Z. Ghassemlooy, S. Rajbhandari, I. Papakonstantinou, and W. Popoola, "Visible light communications: 170 Mb/s using an artificial neural network equalizer in a low bandwidth white light configuration," *Journal of Lightwave Technology*, vol. 32, no. 9, pp. 1807–1813, 2014.

[18] X. Chen and M. Jiang, "Adaptive statistical Bayesian MMSE channel estimation for visible light communication," *IEEE Transactions on Signal Processing*, vol. 65, no. 5, pp. 1287–1299, 2016.

[19] H. Lee, T. Q. Quek, and S. H. Lee, "A deep learning approach to universal binary visible light communication transceiver," *IEEE Transactions on Wireless Communications*, vol. 19, no. 2, pp. 956–969, 2019.

[20] H. Lee, I. Lee, and S. H. Lee, "Deep learning based transceiver design for multi-colored VLC systems," *Optics express*, vol. 26, no. 5, pp. 6222–6238, 2018.

[21] T. Wang, F. Yang, and J. Song, "Deep learning-based detection scheme for visible light communication with generalized spatial modulation," *Optics Express*, vol. 28, no. 20, pp. 28 906–28 915, 2020.

[22] X. Yang, Z. Min, T. Xiongyan, W. Jian, and H. Dahai, "A post-processing channel estimation method for DCO-OFDM visible light communication," in *2012 8th International Symposium on Communication Systems, Networks Digital Signal Processing (CSNDSP)*, 2012, pp. 1–4.

[23] T. Zhang, S. Guo, and H. Chen, "Enhancing the bit error rate of visible light communication systems using channel estimation and channel coding," in *Wireless communications, networking and applications*. Springer, 2016, pp. 51–58.

[24] J. Carruthers and P. Kannan, "Iterative site-based modeling for wireless infrared channels," *IEEE Transactions on Antennas and Propagation*, vol. 50, no. 5, pp. 759–765, 2002.

[25] M. T. Niaz, F. Imdad, W. Ejaz, and H. S. Kim, "Compressed sensing-based channel estimation for ACO-OFDM visible light communications in 5G systems," *EURASIP Journal on Wireless Communications and Networking*, vol. 2016, no. 1, pp. 1–14, 2016.

[26] M. G. Ulkar, T. Baykas, and A. E. Pusane, "VLCnet: Deep learning based end-to-end visible light communication system," *Journal of Lightwave Technology*, vol. 38, no. 21, pp. 5937–5948, 2020.

[27] X. Shi, S.-H. Leung, and J. Min, "Adaptive least squares channel estimation for visible light communications based on tap detection," *Optics Communications*, vol. 467, p. 125712, 2020.

[28] J. Du, H. Deng, X. Qian, and C. Zhang, "Channel estimation scheme based on compressed sensing and parameter estimation for an orthogonal frequency division multiplexing visible light communications system," *Optical Engineering*, vol. 55, no. 11, p. 116109, 2016.

[29] H. Zhao, M. Li, R. Wang, Y. Liu, and D. Song, "Compressed sensing theory-based channel estimation for optical orthogonal frequency division multiplexing communication system," *Optics Communications*, vol. 326, pp. 94–99, 2014.

[30] X. Shen, X. Tang, B. Lin, Q. Lai, and J. Xu, "Experimental demonstration of compressed sensing-based channel estimation for OFDM-VLC," in *Asia Communications and Photonics Conference*. Optical Society of America, 2019, pp. M4A–7.

[31] Y. S. Hussein, M. Y. Alias, and A. A. Abdulkafi, "On performance analysis of LS and MMSE for channel estimation in VLC systems," in *2016 IEEE 12th International Colloquium on Signal Processing Its Applications (CSPA)*, 2016, pp. 204–209.

[32] H. Dogan, O. Şaylı, and E. Panayirci, "Pilot assisted channel estimation for asymmetrically clipped optical OFDM over visible light channels," in *2016 IEEE International Black Sea Conference on Communications and Networking (BlackSeaCom)*, 2016, pp. 1–4.

[33] C. Chen, W.-D. Zhong, and L. Zhao, "Sparse Bayesian RVM regression based channel estimation for IM/DD OFDM-VLC systems with reduced training overhead," in *2017 IEEE International Conference on Communications Workshops (ICC Workshops)*. IEEE, 2017, pp. 162–167.

[34] O. Şayli, H. Doğan, and E. Panayirci, "On channel estimation in DC biased optical OFDM systems over VLC channels," in *2016 International Conference on Advanced Technologies for Communications (ATC)*. IEEE, 2016, pp. 147–151.

[35] H. XiaoLi, L. YongWei, Q. Ling, W. FengYing, and G. Tao, "Research on channel estimation algorithm of visible light ACO-OFDM system," in *2021 19th International Conference on Optical Communications and Networks (ICOCN)*. IEEE, 2021, pp. 1–3.

[36] E. B. Bektas and E. Panayirci, "Sparse channel estimation with clipping noise in DCO-OFDM based VLC systems," in *2020 IEEE International Black Sea Conference on Communications and Networking (BlackSeaCom)*, 2020, pp. 1–5.

[37] V. B. Manur and L. Ali, "Compressed sensing channel estimation for STBC-SM based hybrid MIMO-OFDM system for visible light communication," *International Journal of Communication Systems*, vol. 33, no. 11, p. e4403, 2020.

[38] S. Srivastava, C. S. K. Patro, A. K. Jagannatham, and L. Hanzo, "Sparse, group-sparse, and online Bayesian learning aided channel estimation for doubly-selective mmwave hybrid MIMO OFDM systems," *IEEE Transactions on Communications*, vol. 69, no. 9, pp. 5843–5858, 2021.

[39] S. Srivastava and A. K. Jagannatham, "MSBL-based simultaneous sparse channel estimation in SC wideband mmwave hybrid MIMO systems," in *GLOBECOM 2020-2020 IEEE Global Communications Conference*. IEEE, 2020, pp. 1–6.

[40] T. Van Luong, X. Zhang, L. Xiang, T. M. Hoang, C. Xu, P. Petropoulos, and L. Hanzo, "Deep learning-aided optical IM/DD OFDM approaches the throughput of RF-OFDM," *IEEE Journal on Selected Areas in Communications*, vol. 40, no. 1, pp. 212–226, 2021.

[41] X. Zhang, Z. Babar, R. Zhang, S. Chen, and L. Hanzo, "Multi-class coded layered asymmetrically clipped optical OFDM," *IEEE Transactions on Communications*, vol. 67, no. 1, pp. 578–589, 2018.

[42] B. G. Guzmán, V. P. G. Jiménez, M. C. Aguayo-Torres, H. Haas, and L. Hanzo, "Downlink performance of optical OFDM in outdoor visible light communication," *IEEE Access*, vol. 6, pp. 76 854–76 866, 2018.

[43] R. Singh, T. O'Farrell, and J. P. David, "An enhanced color shift keying modulation scheme for high-speed wireless visible light communications," *Journal of Lightwave Technology*, vol. 32, no. 14, pp. 2582–2592, 2014.

[44] Z. Ghassemlooy, W. Popoola, and S. Rajbhandari, *Optical wireless communications: system and channel modelling with Matlab®*. CRC press, 2019.

[45] Z. Babar, X. Zhang, P. Botsinis, D. Alanis, D. Chandra, S. X. Ng, and L. Hanzo, "Near-capacity multilayered code design for LACO-OFDM-aided optical wireless systems," *IEEE Transactions on Vehicular Technology*, vol. 68, no. 4, pp. 4051–4054, 2019.

[46] R. Zhang, H. Claussen, H. Haas, and L. Hanzo, "Energy efficient visible light communications relying on amorphous cells," *IEEE Journal on Selected Areas in Communications*, vol. 34, no. 4, pp. 894–906, 2016.

[47] J. Beysens, Q. Wang, and S. Pollin, "Exploiting blockage in VLC networks through user rotations," *IEEE Open Journal of the Communications Society*, vol. 1, pp. 1084–1099, 2020.

[48] S. K. Wilson and J. Holliday, "Scheduling methods for multi-user optical wireless asymmetrically-clipped OFDM," *Journal of Communications and Networks*, vol. 13, no. 6, pp. 655–663, 2011.

[49] H. Minn and V. K. Bhargava, "An investigation into time-domain approach for OFDM channel estimation," *IEEE Transactions on Broadcasting*, vol. 46, no. 4, pp. 240–248, 2000.

[50] V. Jungnickel, V. Pohl, S. Nonnig, and C. Von Helmolt, "A physical model of the wireless infrared communication channel," *IEEE Journal on Selected Areas in Communications*, vol. 20, no. 3, pp. 631–640, 2002.

[51] D. Wu, Z. Wang, R. Wang, J. He, Q. Zuo, and H. Zhao, "Channel estimation for asymmetrically clipped optical orthogonal frequency division multiplexing optical wireless communications," *IET communications*, vol. 6, no. 5, pp. 532–540, 2012.

[52] H. Elgala, R. Mesleh, and H. Haas, "Practical considerations for indoor wireless optical system implementation using OFDM," in *2009 10th International Conference on Telecommunications*, 2009, pp. 25–29.

[53] S. M. Kay, *Fundamentals of statistical signal processing: estimation theory*. Prentice-Hall, Inc., 1993.

[54] E. Crespo Marques, N. Maciel, L. Naviner, H. Cai, and J. Yang, "A review of sparse recovery algorithms," *IEEE Access*, vol. 7, pp. 1300–1322, 2019.

[55] M. E. Davies and Y. C. Eldar, "Rank awareness in joint sparse recovery," *IEEE Transactions on Information Theory*, vol. 58, no. 2, pp. 1135–1146, 2012.

[56] J. A. Tropp and A. C. Gilbert, "Signal recovery from random measurements via Orthogonal Matching Pursuit," *IEEE Transactions on Information Theory*, vol. 53, no. 12, pp. 4655–4666, 2007.

[57] D. Wipf and B. Rao, "Sparse Bayesian learning for basis selection," *IEEE Transactions on Signal Processing*, vol. 52, no. 8, pp. 2153–2164, 2004.

[58] M. E. Tipping, "Sparse Bayesian learning and the relevance vector machine," *Journal of Machine Learning Research*, vol. 1, no. Jun, pp. 211–244, 2001.

[59] I. F. Gorodnitsky and B. D. Rao, "Sparse signal reconstruction from limited data using FOCUSS: A re-weighted minimum norm algorithm," *IEEE Transactions on signal processing*, vol. 45, no. 3, pp. 600–616, 1997.

[60] C. Daskalakis, C. Tzamos, and M. Zampetakis, "Ten steps of EM suffice for mixtures of two Gaussians," in *Conference on Learning Theory*. PMLR, 2017, pp. 704–710.

[61] H. L. Van Trees and K. L. Bell, "Bayesian bounds for parameter estimation and nonlinear filtering/tracking," *AMC*, vol. 10, p. 12, 2007.

[62] V. Mordachev and S. Loyka, "On node density - outage probability tradeoff in wireless networks," *IEEE Journal on Selected Areas in Communications*, vol. 27, no. 7, pp. 1120–1131, 2009.

[63] A. S. Arifin and T. Ohtsuki, "Outage probability analysis in bidirectional full-duplex SISO system with self-interference," in *The 20th Asia-Pacific Conference on Communication (APCC2014)*, 2014, pp. 6–8.

SHUBHAM SAXENA (Graduate Student Member, IEEE) received the B.Tech. degree in Electronics and Communication Engineering from the Dr. A.P.J. Abdul Kalam Technical University, Uttar Pradesh, India, in 2017, and the M.Tech. degree in Communication System Engineering from the Indian Institute of Technology Patna, Patna, India in 2020. He is currently working toward the Ph.D. degree with the Department of Electrical Engineering, Indian Institute of Technology Kanpur, Kanpur, India. His research interests include signal processing and channel learning techniques in 6G wireless systems, Visible Light Communication (VLC), and optical communication systems. He was the joint winner in the Postgraduate category of the MVC All India student paper contest held at the conference IEEE INDICON 2019 and also received the best paper certificate.

SURAJ SRIVASTAVA (Member, IEEE) received the M.Tech. degree in Electronics and Communication Engineering from Indian Institute of Technology Roorkee, India, in 2012, and Ph.D. degree in Electrical Engineering from Indian Institute of Technology Kanpur, India, in 2022. From July 2012 to November 2013, he was employed as a Staff-I systems design engineer with Broadcom Research India Pvt. Ltd., Bangalore, and from November 2013 to December 2015, he was employed as a lead engineer with Samsung Research India, Bangalore where he worked on developing layer-2 of the 3G UMTS/WCDMA/HSDPA modem. His research interests include applications of Sparse Signal Processing in 5G Wireless Systems, mmWave and Tera-Hertz Communication, Orthogonal Time-Frequency Space (OTFS), Joint Radar and Communication (RadCom), Optimization and Machine Learning. He was awarded Qualcomm Innovation Fellowship (QIF) in year 2018 and 2022 from Qualcomm. He was also awarded Outstanding Ph.D. Thesis and Outstanding Teaching Assistant awards from IIT Kanpur. Currently, he is working as a senior lead engineer in Qualcomm India Pvt. Ltd., Bangalore.

SAURABH SHARMA received the B.Tech. degree in Electronics and Communication Engineering (ECE) from Gurukula Kangri Vishwavidyalaya, Haridwar, India, in 2017. He is currently working toward the M.S. (Research) degree in Electrical Engineering (EE) from the Indian Institute of Technology Kanpur, Kanpur, India, specializing in signal processing, communication, and networks. His research interests include Visible Light Communication (VLC), applications of sparse signal processing in optical OFDM systems, 5G and beyond wireless technologies.

ADITYA K. JAGANNATHAM (Senior Member, IEEE) received the bachelor's degree from the Indian Institute of Technology, Bombay, and the M.S. and Ph.D. degrees from the University of California at San Diego, San Diego, CA, USA. From April 2007 to May 2009, he was employed as a Senior Wireless Systems Engineer with Qualcomm Inc., San Diego, where he was a part of the Qualcomm CDMA Technologies (QCT) Division. He is currently a Professor with the Department of Electrical Engineering, IIT Kanpur, where he also holds the Arun Kumar Chair Professorship. His research interests include next generation wireless cellular and WiFi networks, with a special emphasis on various 5G technologies such as massive MIMO, mmWave MIMO, FBMC, NOMA, as well as emerging 6G technologies such as OTFS, IRS, THz systems and VLC. He has been twice awarded the P. K. Kelkar Young Faculty Research Fellowship for excellence in research, received multiple Qualcomm Innovation Fellowships (QIF 2018, 2022), the IIT Kanpur Excellence in Teaching Award, the CAL(IT)2 Fellowship at the University of California at San Diego, the Upendra Patel Achievement Award at Qualcomm San Diego and the Qualcomm 6G UR India gift.

LAJOS HANZO (FIEEE'04) received Honorary Doctorates from the Technical University of Budapest (2009) and Edinburgh University (2015). He is a Foreign Member of the Hungarian Science-Academy, Fellow of the Royal Academy of Engineering (FREng), of the IET, of EURASIP and holds the IEEE Eric Sumner Technical Field Award. For further details please see http://www-mobile.ecs.soton.ac.uk/, https://en.wikipedia.org/wiki/Lajos_Hanzo.